
1 Investigation of the climatology of low-level jets over North 2 America in a convection-permitting WRF simulation

3
4 Xiao Ma^{1,2}, Yanping Li^{1,2}, Zhenhua Li¹, Fei Huo¹

5 ¹Global Institute for Water Security, University of Saskatchewan, 11 Innovation Blvd, Saskatoon, SK, S7N 3H5,
6 Canada

7 ²School of Environment and Sustainability, University of Saskatchewan, 117 Science Place, Saskatoon, SK, S7N 5C8,
8 Canada

9 *Correspondence to:* Yanping Li (yanping.li@usask.ca)

10 **Abstract.** In this study, we utilized a high-resolution (4 km) convection-permitting Weather Research Forecasting
11 (WRF) simulation spanning a 13-year period (2000-2013) to investigate the climatological features of Low-level Jets
12 (LLJs) over North America. The 4-km simulation enabled us to represent the effects of orography and the underlying
13 surface on the boundary layer winds better. Focusing on the continental US and the adjacent border regions of Canada
14 and Mexico, this study characterizes the spatial distribution, seasonal patterns, and diurnal fluctuations of
15 northerly/southerly LLJ occurrence frequencies. This paper not only identified several well-known large-scale LLJs
16 in North America, such as the southerly Great Plains LLJ and the summer northerly California coastal LLJ, but also
17 the Quebec northerly LLJ, which gets less focus before. Moreover, the high-resolution simulation revealed climatic
18 characteristics of weaker and smaller-scale LLJs or low-level wind maxima in regions with complex terrains, such as
19 the northerly LLJs in the foothill regions of the Rocky Mountains and the Appalachian during the winter. Additionally,
20 the different thermal and dynamic mechanisms forming significant LLJs near the Great Plains, California, and Quebec
21 are investigated. This study provides valuable insights into the climatological features of LLJs in North America and
22 the high-resolution simulation offers a more detailed understanding of LLJ behavior near complex terrains and other
23 smaller-scale features.

25 1. Introduction

26 A low-level jet (LLJ) is described as the fast-moving air ribbon located in the lower atmosphere most of the time
27 (Bonner, 1968; Rife et al., 2010). Many of the world's LLJs have been studied, such as the Great Plains LLJ over the
28 central US (Bonner, 1968; Zhong et al., 1996), the Somali LLJ over eastern Africa (Munday et al., 2021), and the
29 South American LLJ over the east Andes Mountains (Montini et al., 2019). Other studies extend beyond in-land LLJs
30 to encompass offshore coastal LLJs such as the California LLJs (Parish, 2000) and North African Coastal LLJ (Soares
31 et al., 2018). A kind of mesoscale weather system, an LLJ has a relatively small vertical range of usually only a few
32 hundred meters, but its width can reach several hundred kilometers. LLJs are closely related to precipitation and even
33 extreme events, and they can transfer abundant water vapor to the downwind regions, providing favorable dynamic
34 conditions for rainfall (Walters and Winkler, 2001; Hodges and Pu, 2019). Meanwhile, researchers have long been
35 interested in investigating their features, because LLJs also affect various processes such as wind power development,
36 air pollution transportation, and urban heat islands: the wind turbines would be influenced by positive wind shear and
37 downward entrainment from the LLJs above them, assisting in extracting energy from the strong wind belt inside LLJs
38 (Gadde and Stevens 2021; Ma et al., 2022). LLJ-related horizontal transportation is beneficial to pollutant removal
39 (Sullivan et al. 2017). The LLJs can enhance the turbulent mixing in the boundary layer thereby decreasing the
40 atmospheric stability, helping pollution diffusion, and weakening urban heat island intensity (Hu et al., 2013).

41 Since the mid-20th century, scientists have used regular rawinsonde observations to investigate the characteristics of
42 LLJs. Applying rawinsondes to investigate the Great Plains LLJ in the central US, Bonner (1968), Mitchell et al.
43 (1995), and Walters et al. (2008) studied its distribution, seasonal activity, horizontal and vertical structure, and diurnal
44 features and established the climatology of the Great Plains LLJ during warm seasons. As well as rawinsondes, radar
45 systems and wind profilers are useful tools for characterizing LLJs. Frisch et al. (1992) observed a typical LLJ process
46 using Doppler weather radar in North Dakota and identified that the friction on the surface of the boundary layer is
47 important in the early stages of LLJ development. Using long-term wind profiler measurement, Miao et al. (2018)
48 interpreted the climatology of LLJs in Beijing and Guangzhou, concluding that the frequency values of LLJs in these
49 two cities are 13.0% and 4.9%, respectively. Moreover, Smith et al. (2019) used the Plains Elevated Convection at
50 Night (PECAN) observations to conduct high-quality measurements of nocturnal LLJs with wide spatial and temporal
51 resolutions. They found that sudden changes in LLJ structure typically result from the spatial evolution of the LLJ.

52 However, there are some disadvantages of observational research that should be noted. First, regular rawinsonde data
53 only contain measurements at two daily time points (00 UTC and 12 UTC), which cannot fully capture LLJs' diurnal
54 variations. The time density of observations is therefore coarse, and coastal areas lack regular high-density
55 measurements, making the study of coastal LLJs challenging (Mitchell et al., 1995). Second, heterogeneities in the
56 rawinsonde records, such as variations in station locations, radiosonde types, and archiving procedures, may also
57 complicate the use of these observations in climate research. Third, rawinsonde measurements taken at a single point
58 are not able to capture horizontal shear and environmental conditions (Chen et al., 2005). Although observations
59 platforms such as radar or field projects like PECAN can compensate to some extent for this lack of observational
60 data, these approaches are still limited by the spatial coverage of their measurement platforms (Smith et al., 2019).

61 Because of these problems with observational methods, researchers have chosen reanalysis datasets as an alternative
62 for investigating LLJs. Reanalysis data have relatively better spatial and temporal coverage than rawinsonde
63 measurements, incorporate observations into the preliminary model simulations, provide more comprehensive
64 variables through assimilation, and contain broader domains. Rife et al. (2010) highlighted the global distribution of
65 identified nocturnal LLJs using reanalysis data with a horizontal grid spacing of 40 km, and even successfully
66 extracted some previously unknown jets, like Tarim nocturnal LLJ in northwest China, Ethiopia nocturnal LLJ, and
67 Namibia–Angola nocturnal LLJ. Doubler et al. (2015) applied the North American Regional Reanalysis (NARR)
68 dataset (~32 km) to generate long-term LLJ climatology in North America. Consistent with previous records,
69 Doubler's results supplemented the description of some smaller-scale LLJs. Similarly, Montini et al. (2019) compared
70 and validated the performance of five different reanalysis datasets in identifying LLJs. Their results showed the 38-
71 year climatology of South American LLJs with ERA-Interim data (~79 km).

72 Scientists have also conducted studies based on numerical simulations, which can more accurately represent LLJs than
73 reanalysis data sets, especially in the vertical direction, thereby yielding new insights into LLJs' features. Tang et al.
74 (2017) used an ensemble of dynamically downscaling regional climate simulations to generate the climatology of
75 Great Plains LLJ and predicted that the LLJ will occur more frequently during the nighttime in spring and summer in
76 mid-21st century. Jiménez-Sánchez et al. (2019) conducted a simulation for LLJs over the Orinoco River Basin by
77 dynamic downscaling of the Weather Research and Forecasting model (WRF). The simulation represented the jet
78 streaks better than previous studies within a broader region of wind enhancement and illustrated more detailed diurnal

79 evolution. Nevertheless, most general numerical simulations still represent the convective processes by the
80 parameterization scheme, which generates uncertainty in the results. These issues can be addressed by using
81 convection-permitting models with grid spacing under 5 km that adequately simulate the convections and other small-
82 scale processes (Liu et al., 2017, Li et al., 2019, Kurkute et al., 2020). Convection-permitting modeling describes the
83 underlying surface more accurately than coarse-resolution simulations and reanalysis data and shows ability in
84 investigations of LLJs near complex mountain areas. Du and Chen (2019) analyzed the LLJs over southern China by
85 using 4-km WRF model and revealed a solid relationship between the mesoscale lifting of LLJs and the convection's
86 initiation. They also highlighted the importance of coastal terrain. Overall, the finer-resolution tools tend to show more
87 comprehensive and precise results, offering detailed and accurate references to LLJs.

88 The formation mechanisms of LLJs have been studied extensively by researchers. In explaining the diurnal cycle
89 feature of the Great Plains LLJ, the inertial oscillation theory proposed by Blackadar (1957) and Stensrud (1996)
90 suggests that the LLJ is related to the friction change in the boundary layer. During the night, the jet-core wind is
91 enhanced after decoupling with near-surface friction. Holton (1967) and Parish (2000) developed the thermal wind
92 adjustment theory, which suggests that the horizontal pressure gradient changes because the atmosphere over sloping
93 terrain is warmer or because sea-land contrast influences the diurnal cycle of wind. Additionally, LLJs can also be
94 formed due to synoptic system forcing, as proposed by Uccellini et al. (1987) and Saulo et al. (2007). However,
95 convection-permitting models can help explain how LLJs form because they have precise descriptions of weather
96 systems and underlying orography. Using 4-km simulations, Fu et al. (2018) and Zhang et al. (2019) analyzed the
97 evolution of LLJs over mountainous areas in eastern and southwestern China, respectively. They concluded that
98 inertial oscillation plays a prominent role in and is responsible for the local precipitation peak at a certain time. Besides,
99 Shapiro et al. (2016) argued that the formation of some LLJs may not be impacted by a single factor and that a unified
100 theory analysis is thus required. Thus, a dataset that offers more information must be very popular. All these studies
101 have shown that convection-permitting models, with both finer coverage and resolutions, are a powerful tool for LLJ
102 climatology research.

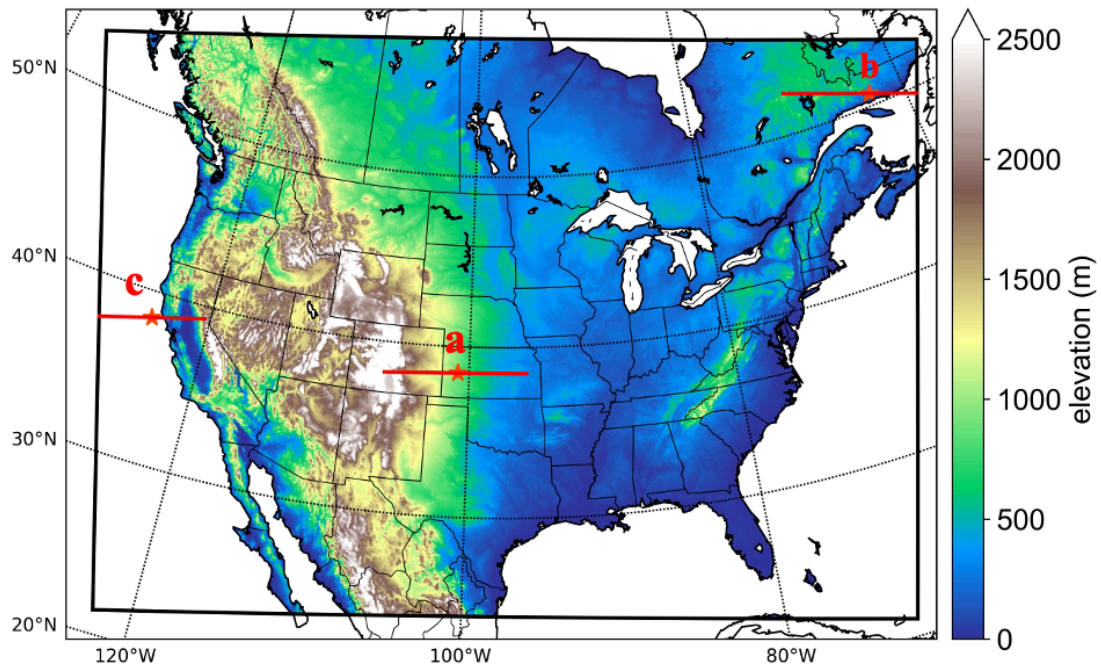
103 In this study, we utilize the 4-km convection-permitting WRF simulation (Liu et al., 2017) to compile a comprehensive
104 LLJ climatology across North America and investigate the features of major LLJ systems in the region with improved
105 spatial and temporal resolutions. Section 2 introduces the model configuration and the criteria for LLJ identification,

106 Section 3 presents the characteristics of LLJ frequencies in North America, and Section 4 illustrates the analysis of
107 the background and mechanisms in several LLJ cases. Finally, Section 5 provides the discussion and conclusion.

108 **2. Model configuration and methods**

109 **2.1 WRF setup**

110 This study utilized a convection-permitting Weather Research and Forecasting (WRF) dataset (Liu et al. 2017, Data
111 available at: <https://rda.ucar.edu/datasets/ds612.0/>) with a horizontal resolution of 4 km over North America, without
112 nesting. The domain covers the entire continental US, Southern Canada, and Northern Mexico, as illustrated in Figure
113 1. The simulation provides three-dimensional data at a temporal resolution of 3 hours, resulting in 8-time steps per
114 day. In the vertical direction, the data have 51 eta levels and can reach 50 hPa. And it should be noted that there are
115 five layers under 500-m height and nine layers under 1 km are outputted above ground level, which means the WRF
116 has the better ability than other coarse modelling, to capture the LLJs occurring in the boundary layer. Considering
117 the computational cost for high-resolution modelling, this simulation period spans from 1st October 2000 to 30th
118 September 2013, and the six-hourly ERA-Interim reanalysis dataset of 0.7° resolution was used as input for the climate
119 simulation, the vertical layer depth of the forcing ERA-Interim data under 5 km is about 0.3-1.4 km (Hoffmann &
120 Spang, 2022). The simulation did not apply any cumulus parameterization scheme due to the fine horizontal grid
121 spacing, but other sub-grid scale processes were parameterized by various physical schemes: the rapid radiative
122 transfer model (RRTMG) (Iacono et al., 2008) was used for simulating longwave and shortwave radiations, the Yonsei
123 University (YSU) scheme was used for representing the planetary boundary layer (Hong et al., 2006), and the Noah-
124 MP model was used for computing surface processes (Niu et al., 2011). In this study, the planetary boundary layer
125 scheme is retained. Nonetheless, it should be noted that this would introduce uncertainties to the simulation in the
126 vertical direction, especially in regions with complex topography.



127
 128 **Figure 1. Study domain of this convection-permitting model. The colors represent the elevation. The red lines and stars**
 129 **show the positions of investigated cross-section and jets in Section 4.**

130

131 **2.2 Methodology**

132 Using the threshold criteria proposed by Bonner (1968), this study identifies LLJs from the vertical wind profile of
 133 each grid point in the model output data. LLJs are present when the following conditions are met: (1) the height of the
 134 LLJ core maximum wind speed is below 3 km above the ground level (AGL); (2) the maximum wind speed is greater
 135 than or equal to 12 m s⁻¹; (3) from the height of the wind maxima to the height of the next minimum value or 3-km
 136 height (whichever is lower), the velocity of winds drop by at least 6 m s⁻¹; (4) the wind speed drops by at least 6 m s⁻¹
 137 below the level of wind maxima. Considering the importance of the meridional LLJ for heat and water vapor
 138 transport, this study addresses their frequencies in different meridional directions. According to Walter et al. (2008)
 139 and Doubler et al. (2015), the criteria for identifying different meridional LLJs are as follows: for southerly LLJs (S-
 140 LLJs), the jet-core wind direction is between 113° and 247°; for northerly LLJs (N-LLJs), the jet-core direction is
 141 between 293° and 67°. These criteria are used in this study.

142 Based on the identification criteria above, we determined if the LLJ existed at each grid point and consequently
 143 counted the occurrences of S-LLJs and N-LLJs. We also calculated the frequencies of LLJs in different seasons or

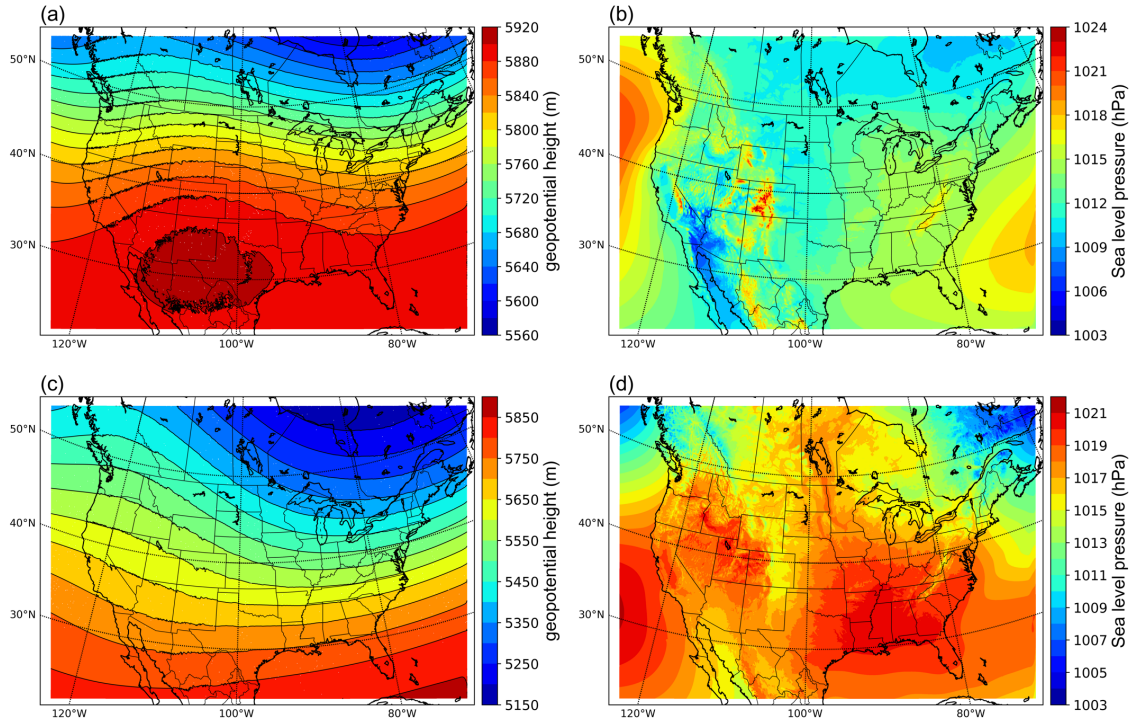
144 time steps. The frequency is defined as the percentage of the total number of occurrences for the selected accumulation
145 period. We generated the frequency distribution maps for LLJs climatology in North America, which are illustrated
146 in Section 3.

147 **3. The climatology of North American LLJs**

148 **3.1 Analysis of atmospheric circulation**

149 This study adopts model data to capture the climatological features of LLJs in North America. Considering the
150 relationship between LLJs and synoptical systems, we evaluated the ability of the convection-permitting model to
151 simulate the background atmospheric circulation. Figure 2 depicts the simulated climatology of geopotential heights
152 at 500 hPa and sea-level pressure isobars for summer and winter. In summer, at a height of 500 hPa (Figure 2a), In
153 summer, the model depicts a trough in the east of the continental US, a ridge over the Rocky Mountains, and the
154 upper-air subtropical anticyclone crossing the southern US. At sea level (Figure 2b), the model captures the Azores
155 High-Pressure area in the Atlantic Ocean and the Hawaiian High-Pressure area in the Pacific.

156 In winter, the contours at the pressure value of 500 hPa (Figure 2c) show stronger fluctuating characteristics: the
157 eastern trough and western ridge over the continent strengthen, and the polar vortex extends to the northern US, while
158 most of North America is controlled by a cold high-pressure system. In addition, the subtropical anticyclone is too
159 weak to be found within the study domain. On the other hand, most of North America is controlled by a cold high-
160 pressure system at sea level (Figure 2d), and parts of the Icelandic Low and Aleutian Low appear on both east and
161 west of Canada, even though their centers are not captured in the domain. To summarize, the convection-permitting
162 model can simulate the features of semi-permanent centers of atmospheric circulations in North America, thus
163 demonstrating its strength in identifying the LLJs in this area.



164
 165 **Figure 2. Climatology of atmospheric circulations simulated by the convection-permitting model: (a) summer 500 hPa**
 166 **geopotential height; (b) sea-level pressure in summer; (c)-(d) the same variables but in winter.**

167

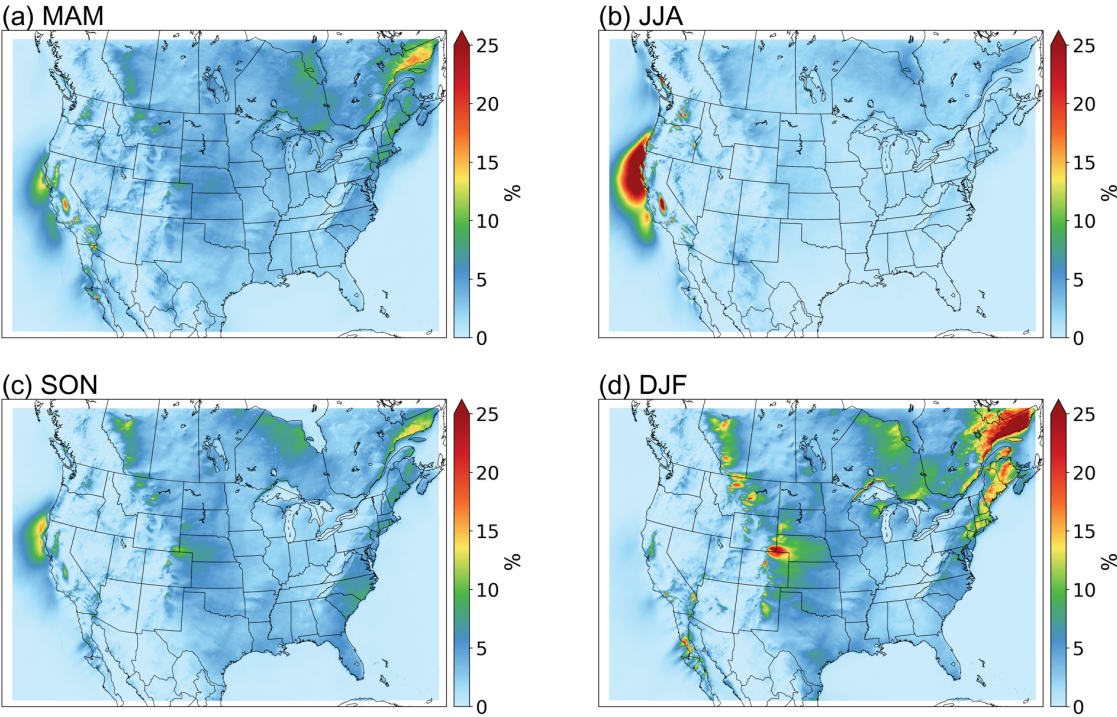
168 3.2 Seasonal variations of LLJs

169 3.2.1 Northerly LLJs

170 Figure 3 shows the frequency distribution of N-LLJ in four seasons, in which the frequency represents the ratio
 171 between the seasonal total number of LLJs occurrence and the total time steps in each season. Clearly, the California
 172 coastal LLJ is strongest in summer (June, July, and August (JJA)), with a large area of N-LLJ frequency greater than
 173 25%, extending from the southern Oregon coast to the central California coast. Regions with a frequency greater than
 174 5% can even extend to the Pacific Ocean near northern Baja California. However, from summer to autumn (September,
 175 October, and November (SON)), the frequency of this LLJ decreases sharply, with a frequency of only 5%-15% in
 176 the core region, and it is only distributed on the northern coast of California. In winter (Dec, Jan, and Feb (DJF)) it
 177 occurs very infrequently (~3%).

178 On the other hand, various N-LLJ phenomena occur frequently in the cold season. These N-LLJs are mainly located
 179 near the eastern slopes of special terrains such as the Rocky Mountains, Appalachian Mountains, and the Quebec

180 Labrador Plateau. In winter, high frequencies ($>10\%$) are observed from western Alberta to Oklahoma, within which
181 hot spots are distributed sporadically in Alberta, Montana, Wyoming, and Colorado. These hot spots have frequencies
182 of about 20%, especially in the region between Colorado and Wyoming. In over 25% of the wind profiles, the N-LLJs
183 can even be extracted. The N-LLJs over the Eastern US coast mainly extend from Maine to South Carolina, and their
184 highest frequency can reach about 15%-20%. The N-LLJs in eastern Quebec also occur most frequently in winter
185 ($>25\%$). Over Hudson Bay, the simulation can also detect the N-LLJ from about 10% of the time steps. The
186 frequencies of all the N-LLJs mentioned above decline significantly in spring, and it is hard to detect them in summer
187 as the frequencies are mostly less than 5%.



188
189 **Figure 3. Seasonal occurrence frequency of N-LLJs. Frequency shown here is calculated by counting the number of**
190 **occurrences of LLJs in each three-hourly time step and then dividing the total number of LLJs in each season**
191 **of time steps in that season.**

192 **3.2.2 Southerly LLJs**

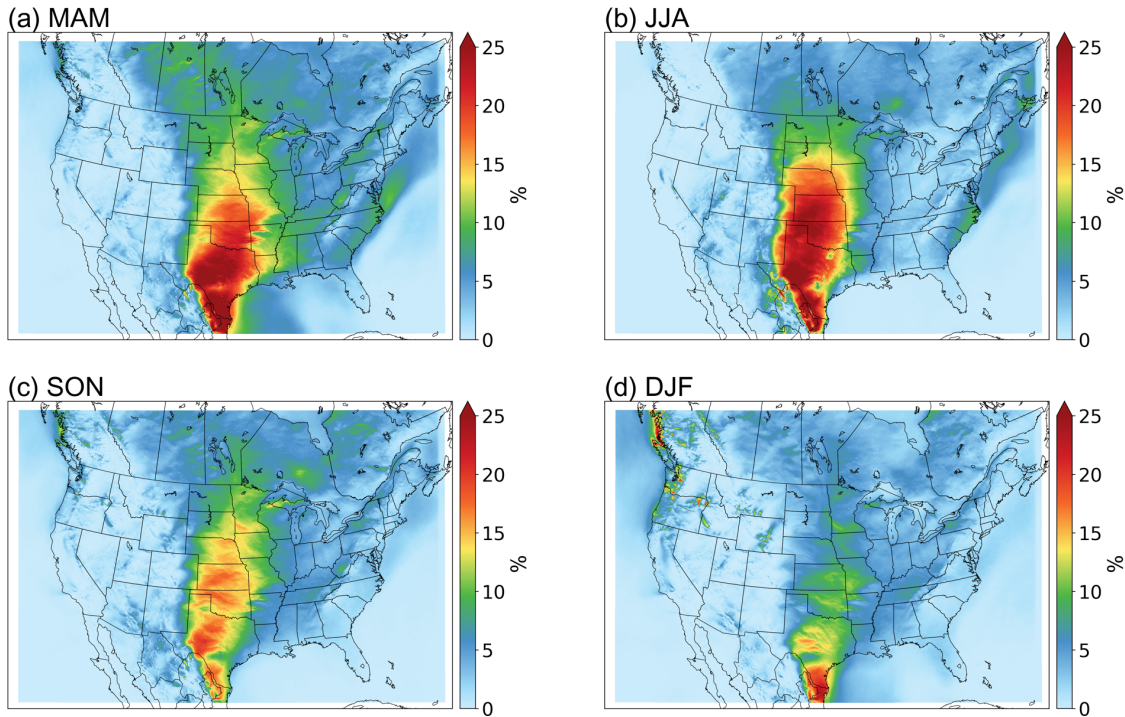
193 As to the climatology of S-LLJs in different seasons (see Figure 4), in winter, in the broad region extending from the
194 south Texas-west Gulf of Mexico to southern Iowa, the frequencies of S-LLJs exceed 10%. The greatest frequencies
195 of S-LLJs ($>20\%$) are found along the border between northeastern Mexico and the United States. In addition, about

196 15% of the simulated wind profiles in south-central Texas are identified as S-LLJs. In the spring (March, April, and
197 May), the frequency expands significantly in >10% of areas, with clear S-LLJ distributions detected in Manitoba,
198 Saskatchewan, and other parts of Canada. The highest frequencies are still found in the Texas-Mexico area, where the
199 magnitude of these frequencies increases to over 25%. This region also extends northward to occupy most of Texas.
200 In winter, S-LLJs with occurrence frequencies of above 15% extend to near Colorado and Nebraska.

201 In summer, the area with frequencies greater than 10% no longer extends to the central Canadian prairie provinces
202 and Tennessee. The S-LLJs over the western Gulf of Mexico are also difficult to identify with modeled data, and their
203 frequency is close to 0%. In contrast, the area with frequencies exceeding 25% extends northward in summer and is
204 roughly divided into three parts distributed respectively in the northeast Mexico-Texas border, west-central Texas,
205 and the central US Great Plains (western Oklahoma and southern Kansas). The regions where more than 15% of the
206 wind profiles are identified as S-LLJ also expand from Colorado to near South Dakota.

207 In the fall, the magnitude of the frequency of S-LLJs decreases dramatically in the central US Plains and Texas. The
208 frequency still maintains a level greater than 15% in most areas, but with a maximum frequency of only 20% and
209 sporadically located in southwest Texas. The frequencies greater than 10% again expand northward and eastward in
210 this season, reaching Manitoba and Ontario.

211 There are also several S-LLJs on a smaller scale that can be seen on the seasonal S-LLJ climatology map. In spring, a
212 narrow region of S-LLJs with a frequency greater than 5% on the eastern side of the Appalachians extends from
213 Georgia through the western Atlantic to southern Nova Scotia. Over the Atlantic near eastern Maryland, the frequency
214 of the S-LLJ can exceed 10%. In summer, this narrow frequency belt still exists and has the same coverage, but the
215 magnitude of the frequency decreases and the frequency >10% is no longer visible. In winter, a region where S-LLJ
216 frequency is >5% extends from southwest Oregon to the west coast of British Columbia of Canada. But in spring, S-
217 LLJs with frequencies >5% occur only over the ocean west of British Columbia. As for the summer, S-LLJs are almost
218 undetectable in this region.



219
220

Figure 4. Seasonal frequency of S-LLJs.

221 To summarize, for the LLJ systems that have been investigated by many researchers, the convection-permitting WRF
 222 model performs well in observing the Great Plains S-LLJ and California coastal N-LLJ during the summer. But as to
 223 the winter LLJs that lack attention, it is essential to compare and validate the occurrence and features revealed by
 224 WRF simulation. Therefore, the ERA5 reanalysis dataset is applied in this study for capturing the LLJs in winter using
 225 the same criterion. Appendix after the text shows the results of the comparison between ERA5 and WRF simulation.

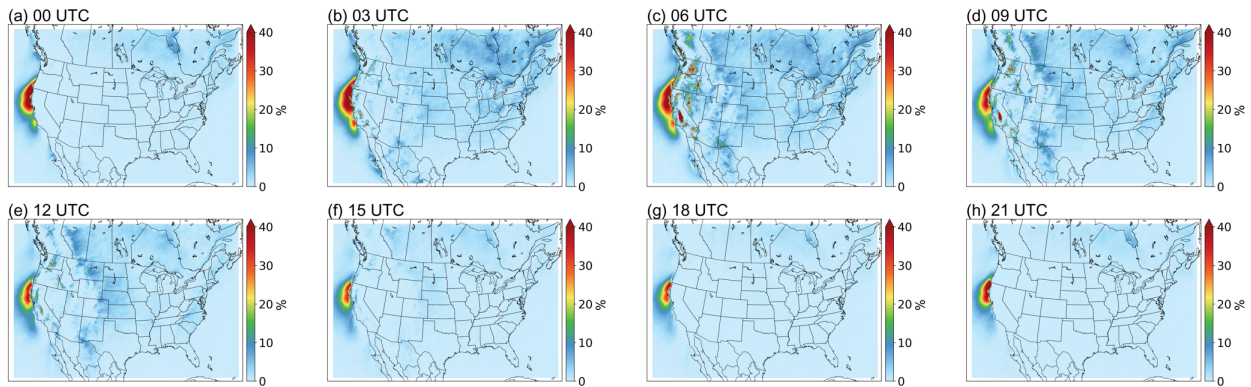
226 3.3 Diurnal variations of LLJs

227 To show the diurnal features of the LLJs, we selected summer and winter as the representative seasons because S-
 228 LLJs and N-LLJs occur most frequently in these seasons, respectively. Below, the descriptions are divided into N-
 229 LLJs and S-LLJs.

230 3.3.1 Northerly LLJs

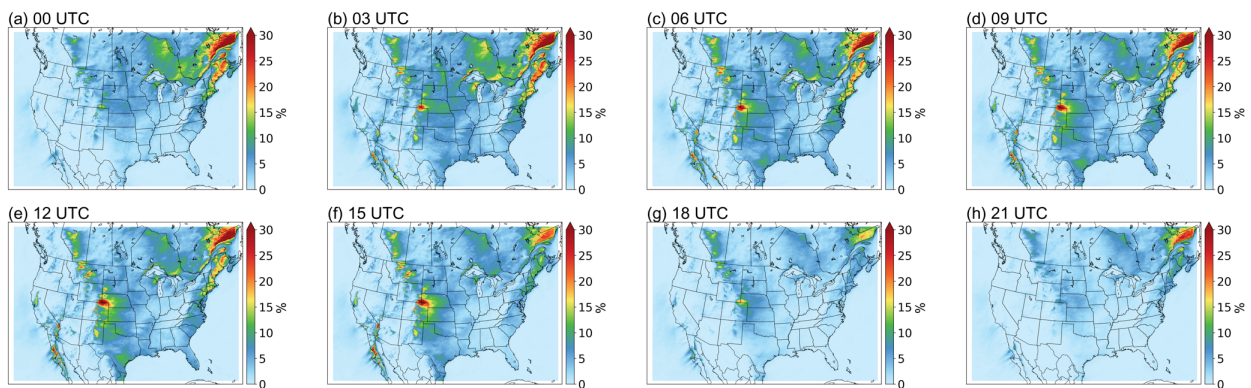
231 The California coastal N-LLJ is the most highlighted low-level jet system in this region in summer. As seen in Figure
 232 5, it occurs throughout the day over the eastern Pacific Ocean from Oregon to the California coast. Figure 5 also shows
 233 that the California Coastal N-LLJ has diurnal characteristics: from 21 UTC (1 pm LST in California), the low-level

234 jet begins to develop, with a N-LLJ frequency of >30%, expanding until it reaches its maximum at 03 UTC – 06 UTC.
 235 Then the high-frequency coverage of the California coastal LLJ gradually shrinks, reaching the minimum at 18 UTC
 236 and only existing off the northwest coast of California.



237
 238 **Figure 5. Diurnal frequency of N-LLJs in the summer (JJA).**

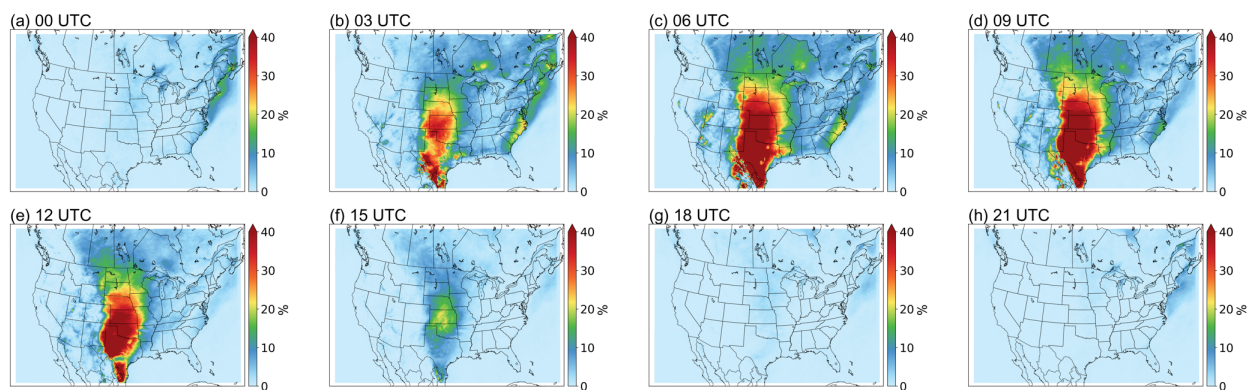
239 In winter (Figure 6), three types of N-LLJs over the Hudson Bay Lowlands, the eastern slopes of the Quebec Labrador
 240 Plateau, and the Appalachians display similar diurnal fluctuations. All three N-LLJs reach their highest frequency at
 241 03 UTC (10 pm EST) and their lowest at 18 UTC (1 pm EST). The only difference among the three types is that the
 242 smallest frequency of the Quebec N-LLJ still endures at a level of greater than 15%, while the other two N-LLJs
 243 mostly have frequencies of about 5%. The smallest frequency (~5%) of N-LLJs occurs downstream of the Rocky
 244 Mountains (over Alberta, Montana, and Kansas) at 21 UTC. In the subsequent development stage, the changes in the
 245 sporadic hot spots distributed near the eastern boundary of the Rocky Mountains are more significant. As seen in
 246 Figure 6, frequency starts growing from 00 UTC and then peaks at 12 UTC, especially the wind maxima located in
 247 Colorado, Wyoming, and Kansas, where the highest frequency can be >25%.



248
 249 **Figure 6. Diurnal frequency of N-LLJs in winter (DJF).**

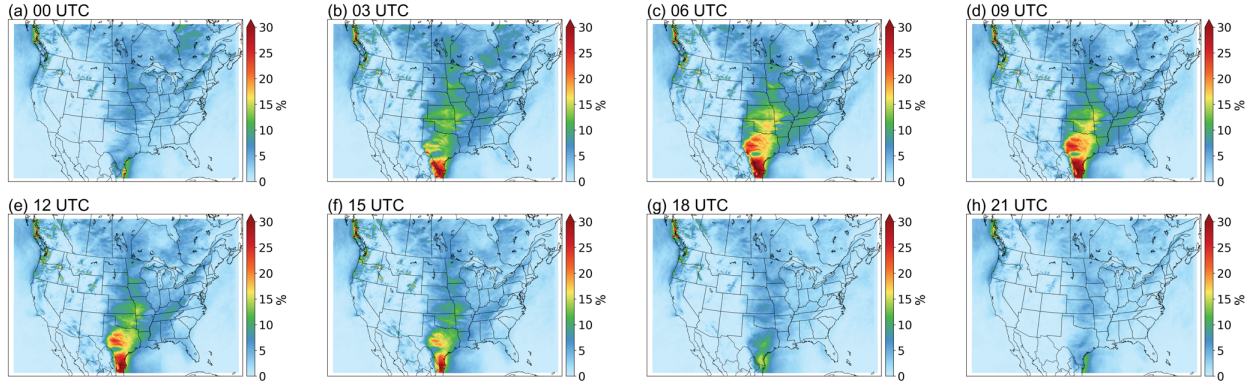
250 3.3.2 Southerly LLJs

251 In summer, the Great Plains S-LLJ occurs more frequently than in other seasons, and its diurnal variability is also the
252 strongest in this season (see Figure 7). At noon local time and in the afternoon (18 UTC – 00 UTC), almost no S-LLJs
253 occur over the central US (frequency <5% or about 0%). In contrast, the Great Plains LLJ begins to develop at 03
254 UTC, when a frequency of over 25% extends from Mexico to Kansas. It reaches maximum strength at midnight (06
255 UTC – 09 UTC), when the frequency reaches over 30% and the high-frequency coverage enlarges to the Dakotas, the
256 border of the eastern Rocky Mountains, and western Minnesota, Missouri, and Louisiana. Summer S-LLJs are also
257 active in southern Canada at night and in the early morning. In Saskatchewan, Manitoba, and central Ontario (03 UTC
258 – 12 UTC, as shown in Figure 7), S-LLJs are found with frequency >15%. In the eastern US and Atlantic, S-LLJs
259 occur most frequently at midnight (03 UTC – 06 UTC).



260
261 **Figure 7. Diurnal frequency of S-LLJs in summer (JJA).**

262 For the cold season (Figure 8), even though the Great Plains LLJ is the most inactive based on the description in
263 section 3.2, it still has a clear diurnal variation. Compared with the results in summer, the diurnal cycle of Great Plains
264 LLJ in winter is not that pronounced: It mainly occurs over the western Gulf of Mexico and southern Texas, with the
265 frequency in the afternoon (18 UTC – 21 UTC) declining to 5-10%. The S-LLJ develops from 03 UTC, gradually
266 generating two high-frequency (20%-25%) centers in mid- and southeastern Texas at 06 UTC – 12 UTC. As for the
267 S-LLJ near Vancouver Island, it is hard to see the diurnal variability: There is only a slight magnitude growth of
268 frequency from the afternoon (00 UTC) to the evening (06 UTC), and the coverage is almost the same.



269
270 **Figure 8. Diurnal frequency of S-LLJs in winter (DJF).**

271
272 **4 Formation and evolution mechanisms of various LLJs**

273 Section 3's results illustrate the climatology of LLJs over North America, particularly their seasonal and diurnal
274 features. To explain the mechanisms, the inertial oscillation theory from Blackadar (1957) is used. Using this theory,
275 we start from the horizontal momentum equations and divide the actual horizontal wind u/v into two components—
276 geostrophic wind u_g/v_g and ageostrophic wind u_a/v_a :

277
$$\frac{d(u_g + u_a)}{dt} = -\frac{1}{\rho} \frac{\partial P}{\partial x} + f(v_g + v_a) \quad (1.1)$$

278
$$\frac{d(v_g + v_a)}{dt} = -\frac{1}{\rho} \frac{\partial P}{\partial y} - f(u_g + u_a) \quad (1.2)$$

279
280 In which ρ is air density, P is pressure, and f is the Coriolis parameter. Assuming the horizontal pressure gradient is
281 fixed, the geostrophic wind is a constant as well, which means $\frac{du_g}{dt} = \frac{dv_g}{dt} = 0$:

282
$$\frac{du_a}{dt} = -\frac{1}{\rho} \frac{\partial P}{\partial x} + f(v_g + v_a) \quad (2.2)$$

283
$$\frac{dv_a}{dt} = -\frac{1}{\rho} \frac{\partial P}{\partial y} - f(u_g + u_a) \quad (2.2)$$

284
285 When the definition of geostrophic wind $u_g = -\frac{1}{\rho f} \frac{\partial P}{\partial y}$ and $v_g = \frac{1}{\rho f} \frac{\partial P}{\partial x}$ is combined, the equation (2) is:

286
$$\frac{du_a}{dt} = f v_a \quad (3.1)$$

287
$$\frac{dv_a}{dt} = -f u_a \quad (3.2)$$

288

289 If $\frac{d}{dt}$ is taken to both sides of the equations (3), then we get $\frac{d^2u_a}{dt^2} = -f^2u_a$, and $\frac{d^2v_a}{dt^2} = -f^2v_a$, thereby:

290
$$u_a = c_1 \cos(ft) + c_2 \sin(ft) \quad (4.1)$$

291
$$v_a = c_2 \cos(ft) - c_1 \sin(ft) \quad (4.2)$$

292

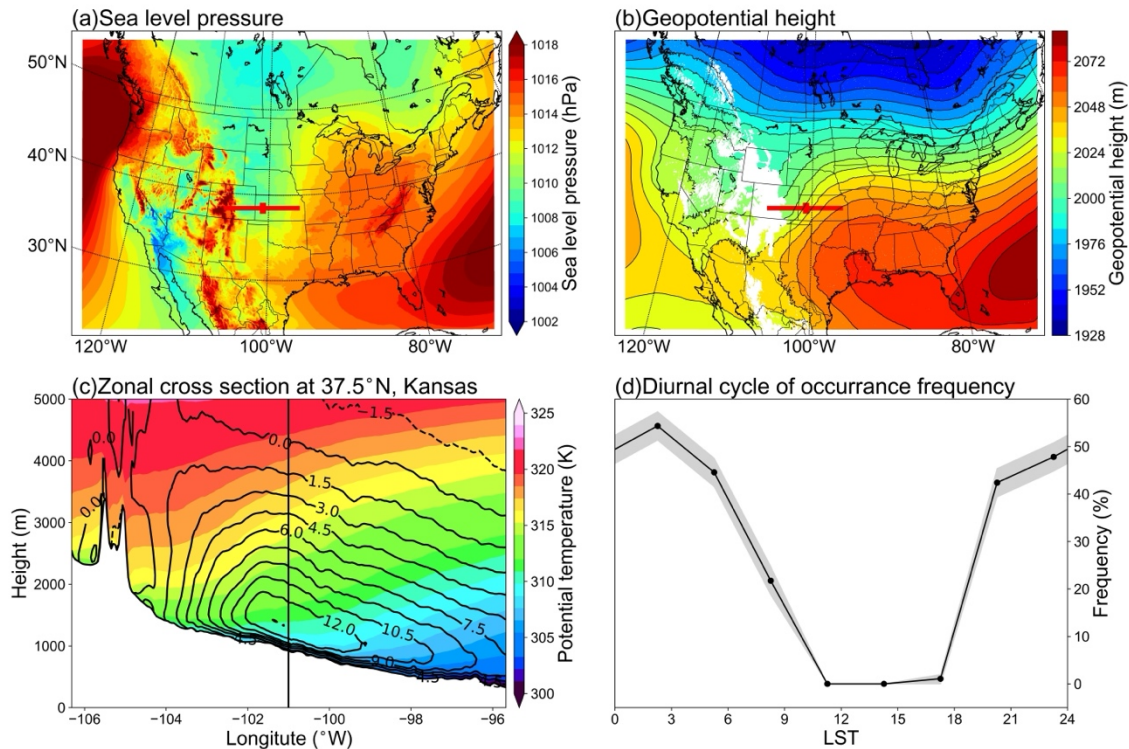
293 Therefore, according to the equations (4), the ageostrophic wind should theoretically have a circle-pattern variation
294 and the vector must rotate clockwise with a period of $2\pi/f$ (Blackadar, 1957; Van de Wiel et al., 2010). Under the
295 condition of a constant geostrophic wind—when the ageostrophic vector rotates from the opposite to the same
296 direction of geostrophic wind—the wind transitions from subgeostrophic to supergeostrophic. This change occurs
297 because of decoupling with surface friction effects, then the wind gets unbalanced.

298 Other theories also help explain the formation of LLJs, such as the sloping-terrain thermodynamic mechanism (Holton,
299 1967) and background synoptic system forcing (Uccellini et al., 1987). To understand the characteristics of the LLJs
300 in this study, three typical cases are analyzed: Great Plains S-LLJ, Quebec N-LLJ, and California coastal N-LLJ. The
301 locations for extracting data are shown in Figure 1 (solid lines and stars a, b, c).

302 **4.1 Great Plains S-LLJ**

303 As Section 3's results show (see Fig. 7), the Great Plains S-LLJ typically occurs in summer and more frequently at
304 night. To investigate its associated meteorological condition, this study extracts all the Great Plains S-LLJ cases occurs
305 at the jet core in JJA. The jet core is defined by where the mean meridional wind is the strongest on the cross-section,
306 and it locates at star A (shown in figure 1). The mean sea-level pressure and 800 hPa geopotential height are shown
307 in Figure 9a and 9b, respectively. The background large-scale circulations indicate that, at all the time points when
308 the Great Plains S-LLJ occurs, the range of the subtropical anticyclone extends east of the Great Plains at both ground
309 and low-level atmosphere. A high-pressure ridge is located near the gulf coast of Mexico and Texas (Figure 9b). Thus,
310 clearly, the zonal pressure/geopotential gradient in the central US guides the dominant southerly winds around this
311 region. The cross-section in Figure 9c illustrates a strong baroclinicity and shows that the isentropic line incline moves
312 from east to west, as is typical for the sloping-terrain heating effect (Holton, 1967). This effect generates an upslope
313 wind on the east side of the slope, and the airstream gradually turns northward due to the Coriolis force, creating the
314 southerly LLJs. On the other hand, as can be seen in the frequency cycle in Figure 9d, at noon local time (at the

315 selected point-a in Figure 1), the frequency of the Great Plains LLJ is very low (close to 0%), rising to more than 40%
 316 after 18 LST even if the radiation is not at the day's peak.



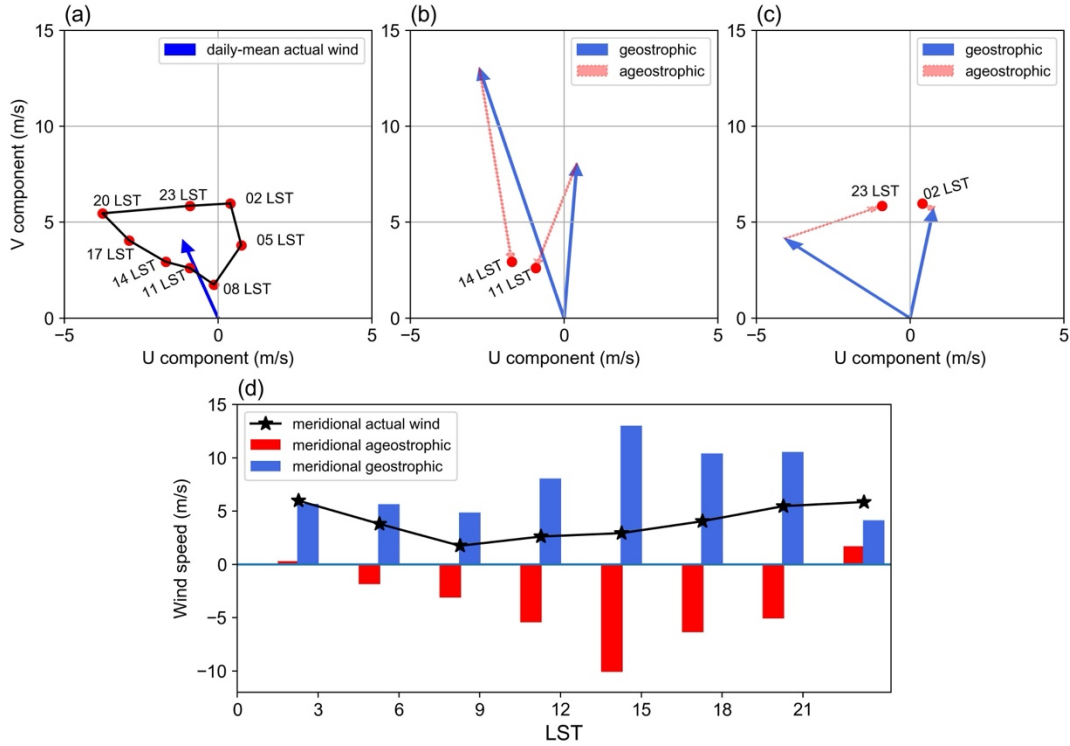
317
 318 **Figure 9. Background circulations of the Great Plains S-LLJ in JJA: (a) sea-level pressure, (b) geopotential height of 800**
 319 **hPa, (c) cross section including meridional winds (lines) and potential temperature (shading), and (d) diurnal cycle of**
 320 **frequency, with the shaded 95% confidence intervals. The red lines and points in (a) and (b) show the position of cross-**
 321 **section and chosen jet core, the vertical line in (c) shows the zonal location of the chosen jet core.**

322 To explain the nighttime enhancement of S-LLJ, we analyzed the wind vectors using inertial oscillation theory. To
 323 show more significant diurnal variation, all the time points, including the LLJs that did not occur, were considered.
 324 Figure 10a is the hodograph of jet-core winds at point-a near the Great Plains, and their temporal mean is computed
 325 at 3-hourly intervals in summer. It is noted here that the “jet-core” means the position where LLJ occurs the most
 326 frequently on the cross-section. Compared with the mean actual wind (blue arrow), the deviation at each local time
 327 shows a clear clockwise rotation. The wind speed begins increasing after 17 LST. Nevertheless, the analysis for Figure
 328 9 indicates the sloping heating effect, meaning that the geostrophic wind is not fixed.

329 Thus, to obtain the ageostrophic winds, we computed the geostrophic components by pressure gradient and subtracted
 330 them from the actual airflow. According to the aforementioned definition of geostrophic wind, u_g and v_g are

331 calculated by the horizontal pressure gradient $\frac{\partial P}{\partial y}$ and $\frac{\partial P}{\partial x}$, respectively. By choosing four grids surrounding point-a, we
332 first interpolated the pressure value to the same level as the LLJ core height. Then, we adopted the central difference
333 equation $\frac{\Delta P}{\Delta x} = \frac{P_{i+1} - P_{i-1}}{x_{i+1} - x_{i-1}}$ or $\frac{\Delta P}{\Delta y} = \frac{P_{i+1} - P_{i-1}}{y_{i+1} - y_{i-1}}$ to obtain the pressure gradients at point-a, where i is the index of the grid
334 point at point-a.

335 Figures 10b and 10c display geostrophic wind vectors (blue arrows) and ageostrophic vectors (pink) at noon and
336 midnight. The southerly geostrophic flows are much stronger in the afternoon (10b) than at midnight. The ageostrophic
337 winds flow mostly in the opposite direction, limiting the actual wind speed. At night (10c), the geostrophic wind
338 direction rotates clockwise from that of the afternoon as the pressure gradient changes. Considering the relative
339 positions of blue and pink vectors at 23 LST and 01 LST, ageostrophic flow has rotated roughly 150 degrees to
340 enhance the geostrophic winds, thereby creating a super-geostrophic state. Although the inertial oscillation theory can
341 help explain some aspects of wind behavior, the real situation is more complex than initially thought. Figures 10b and
342 10c indicate that by 02 LST, the wind is almost entirely geostrophic with only negligible ageostrophic perturbations.
343 This suggests that the diurnal changes in the geostrophic wind and pressure gradient may provide a complicating
344 background that prevents the inertial oscillation theory from fully prevailing. While the inertial oscillation theory can
345 provide valuable insights, it should not be relied upon as the sole explanation for LLJs at the Great Plains. Instead, a
346 more comprehensive understanding of atmospheric dynamics is necessary to fully comprehend the behavior of the
347 wind, particularly when dealing with diurnally changing conditions. Figure 10d compares different meridional wind
348 components' amplitudes. The geostrophic wind contributes significantly to the southerly wind during the day, peaking
349 at 14 LST (blue bars). The northerly ageostrophic wind (red bars) is highest during the day, indicating the strongest
350 negative impact from friction. The meridional ageostrophic component decreases and eventually reverses at 23 LST,
351 showing a process from sub- to super-geostrophic status. In summary, the thermodynamic circulation near the slopes
352 of the Great Plains contributes to the strong southerly airflow, while the inertial oscillation plays a critical role in
353 forming the nocturnal southerly LLJ.



354

355 **Figure 10.** (a) Hodograph of jet-core winds for the Great Plains S-LLJ every 3 hours over the whole JJA (red dots – solid
 356 line) and the daily averaged actual wind velocity (blue vector); vectors of mean jet-core geostrophic winds (solid blue) and
 357 ageostrophic winds (dashed red) at (b) 11/14 LST and (c) 23/02 LST; (d) diurnal cycles of meridional components of actual
 358 (black line), geostrophic (blue bars), and ageostrophic winds (red bars).

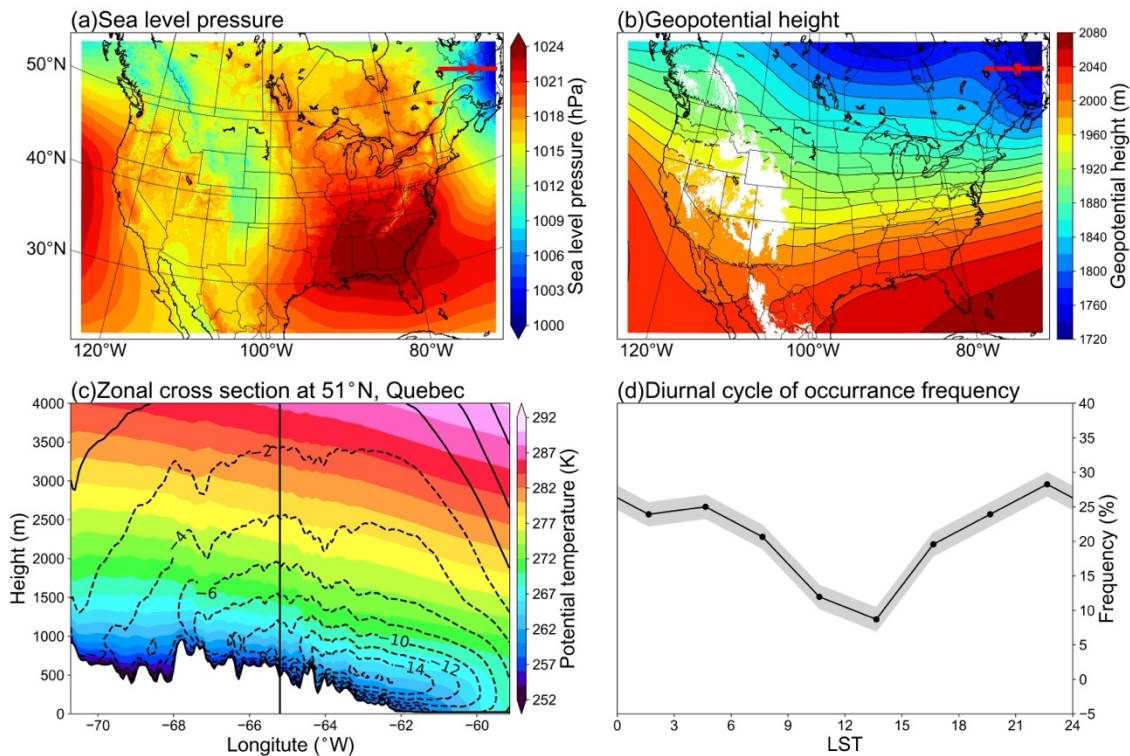
359

360 4.2 Quebec N-LLJ

361 Similarly, for the Quebec N-LLJ that is typically observed in winter, we selected all the LLJ cases at point-b (see the
 362 position in Figure 1) in DJF to generate the background circulation pattern. The background large-scale circulations
 363 indicate that the northeastern coast of Canada lies to the west of a strong surface low-pressure system (Figure 11a),
 364 while in the lower troposphere, a ridge on the east side of Hudson Bay occupies the Labrador Plateau (Figure 11b).
 365 This combination brings the northerly momentum to the downstream eastern coast. In fact, the background circulation
 366 is consistent with the shallow baroclinic structure of Quebec N-LLJ in winter, that is, the thermal difference between
 367 relatively warm sea and cold land. The cross-section in Figure 11c shows the thermodynamic structure of this N-LLJ:
 368 A well-defined low-level jet core is located above land and close to the coastline (approximately 63°W). With a
 369 maximum wind speed of more than 16 m s⁻¹ and a height of about 400 m, the jet core is located above the mixed layer
 370 under the warm air covering and on the land side. Notably, the steep isentropic lines slope towards the ocean and

371 finally sink at the position of 60°W. The onshore isentropic lines are flat and dense above the LLJ core, which means
 372 the environment is quite stable. This is helpful to maintain the structure of the LLJ, when vertical motion is inhibited,
 373 and horizontal wind is enhanced. Compared with the sloped isentropic lines in the Great Plain S-LLJ case (Figure 9c),
 374 the stability over Great Plain is not as high as in this case, so this difference in stability helps explain the variation in
 375 wind speeds between these two cases.

376 In addition, the diurnal cycle of frequency (Figure 11d) shows that the diurnal signal and peak frequency of Quebec
 377 N-LLJ are much weaker than the Great Plains S-LLJ, becoming weakest at noon and peaking at midnight, which is
 378 consistent with the results reported in Section 3. This diurnal variation can be explained by the baroclinicity near this
 379 region: At night in winter, the land temperature drops faster than the ocean temperature due to radiative cooling,
 380 enhancing the land-sea contrast and thereby the thermal wind above. The gentle slope on the east of the Labrador
 381 Plateau could generate the slope heating effect in the daytime. In this way, the related temperature gradient from east
 382 to west offsets the land-sea thermal difference.

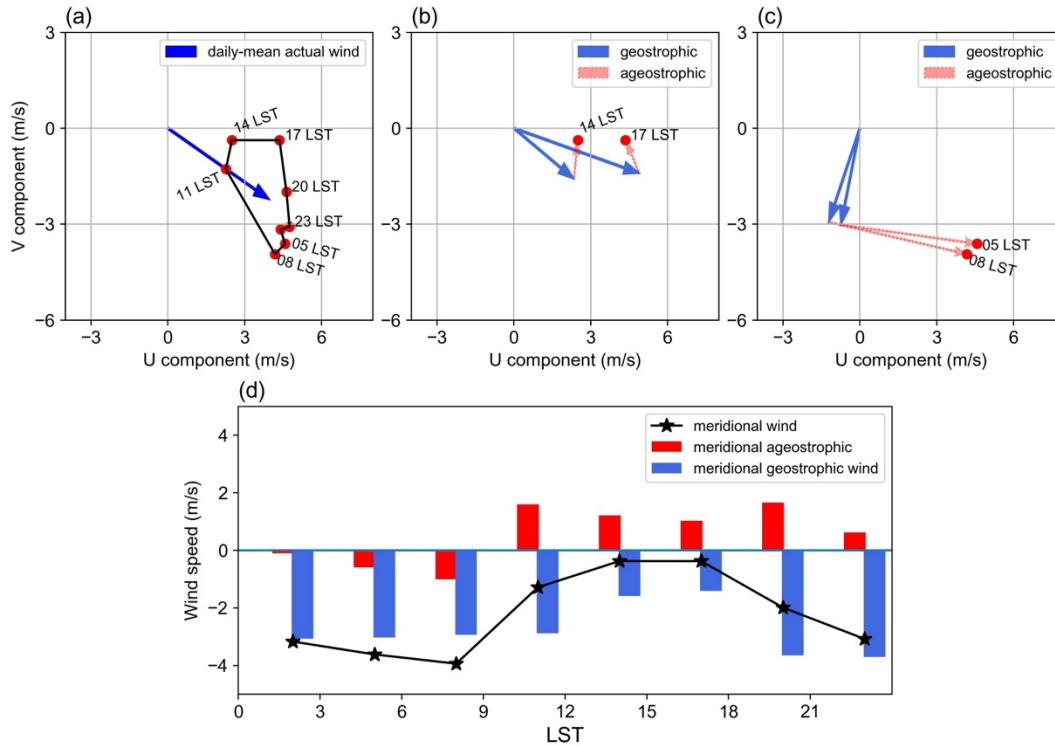


383
 384 **Figure 11. Background circulations of the Quebec N-LLJ in DJF: (a) sea-level pressure, (b) geopotential height of 800 hPa,**
 385 **(c) cross section including meridional winds (lines) and potential temperature (shading), and (d) diurnal cycle of frequency**

386 **with the shaded 95% confidence intervals. The red lines and points in (a) and (b) show the position of cross-section and**
387 **chosen jet core, the vertical line in (c) shows the zonal location of the chose jet core.**

388 As for the impact of inertial oscillation on the Quebec N-LLJ, the hodograph of averaged 3-hourly winds extracted at
389 point-b (Figure 12a) also illustrates a clear clockwise rotation of wind deviations compared with the daily mean (blue
390 arrow). Figure 12b and 12c show that the geostrophic and ageostrophic wind vectors contribute to the diurnal cycle in
391 the afternoon and morning, respectively. Even though the direction of geostrophic wind changes significantly, the
392 relative angles between ageostrophic and geostrophic arrows indicate that the ageostrophic flow rotates clockwise.
393 The geostrophic wind is weakened by ageostrophic wind in the afternoon (Figure 12b), whereas the supergeostrophic
394 state is generated in the morning (Figure 12c).

395 Focusing only on the meridional amplitudes validates this characteristic. In Figure 12d, the blue line that represents
396 the mean actual meridional wind has the same diurnal trend as the frequency variation in Figure 11d. The northerly
397 wind is weakest in the afternoon, peaking at night and in the early morning. Similarly, the variation of meridional
398 geostrophic flow has a consistent phase with the actual meridional wind, which is explained by the baroclinic structure
399 near the Quebec coast mentioned above. The meridional ageostrophic wind in this region also promotes the formation
400 of N-LLJ. The ageostrophic wind drags the geostrophic component in the afternoon, before reversing to a consistent
401 direction with the northerly geostrophic flow at night and in the morning. This trend is also the result of decreasing
402 friction after sunset. Therefore, the evolution of Quebec N-LLJ derives from both inertial oscillation and land-sea
403 thermal contrast in winter.



404
 405 **Figure 12. (a) Hodograph of jet-core winds for the Quebec N-LLJ every 3 hours over the whole DJF (red dots – solid line)**
 406 **and the daily averaged actual wind velocity (blue vector); vectors of mean jet-core geostrophic winds (solid blue) and**
 407 **ageostrophic winds (dashed red) at (b) 14/17 LST and (c) 05/08 LST; (d) diurnal cycles of meridional components of actual**
 408 **(black line), geostrophic (blue bars), and ageostrophic winds (red bars).**

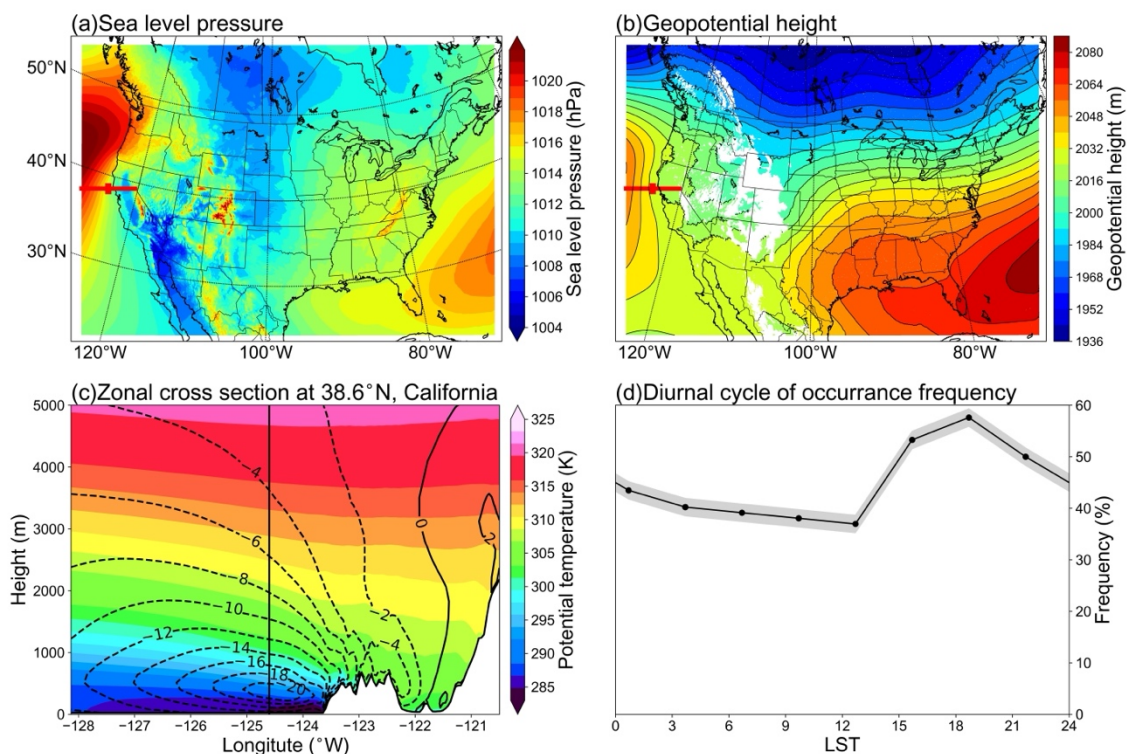
409

410 4.3 California coastal N-LLJ

411 The California coastal N-LLJ is similar to the one in Quebec, but it occurs more often in summer afternoons or
 412 evenings over the ocean. Figure 13a shows that a relatively strong high-pressure system is located on the east coast of
 413 the Pacific Ocean, trending NE-SW, although half of the structure is beyond the boundary of the domain. On the 800
 414 hPa isobaric surface in Figure 13b, there is also an anticyclone system in the same location, whose eastern contour is
 415 roughly parallel to the coastline, guiding the airflow to the south. Therefore, this pair is also forced by the thermal
 416 difference between land and sea, but contrary to the LLJ in Quebec, in summer, when the California LLJ occurs
 417 frequently, it has the characteristics of the cool sea-hot land. Figure 13b also shows that the isobars near Cape
 418 Mendocino are relatively strong, making the ridge of high pressure extend northeastward of the Cape. This extension
 419 is generally believed to occur due to pressure perturbation caused when northerly winds converge at this position after
 420 being obstructed (Rahn and Parish, 2007). Regarding the cross-section structure shown in Figure 13c, the jet core is

421 located at steep isentropic lines above the ocean at a height of 500 m. On the coast of California, the LLJ is close to
422 the mountains. The maximum central wind speed of California coastal LLJ exceeds 20 m s⁻¹, whereas Quebec N-
423 LLJ's max core wind is only about 14 m s⁻¹. Based on baroclinicity, the isentropic lines slope towards the continent
424 and finally sink near the coastline.

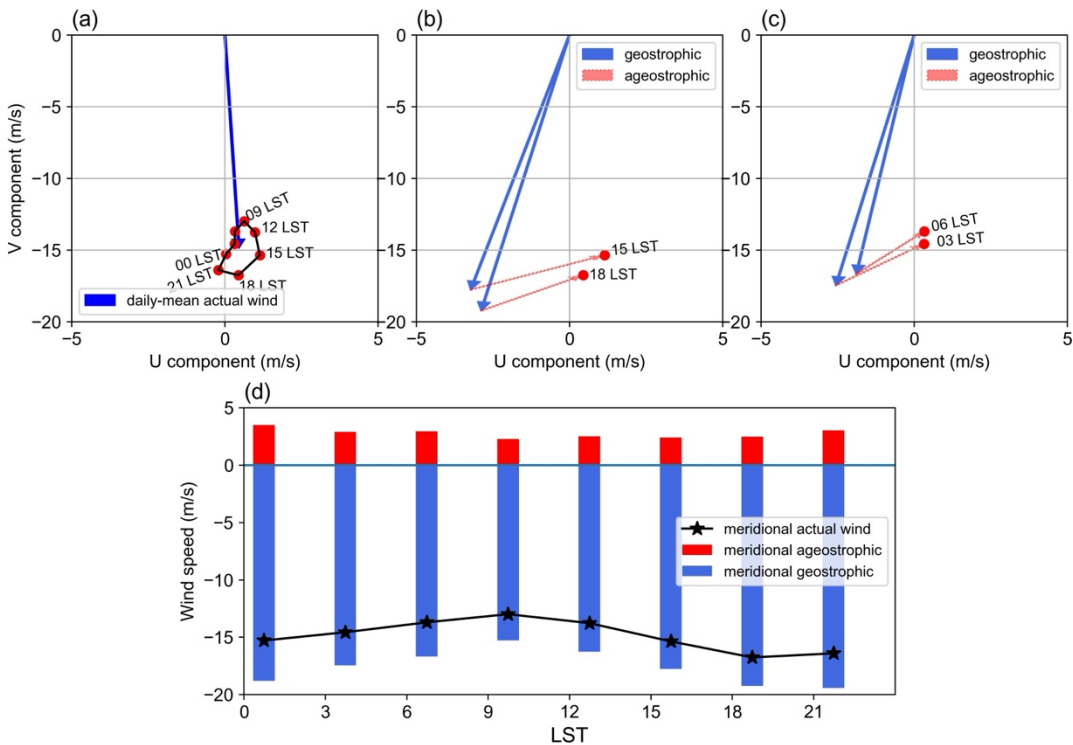
425 The core wind speed in California's coastal LLJ is higher than that of Quebec's LLJ because the land-sea contrast is
426 more significant in summer than in winter and the formed sea breeze front generates flow convergence under the
427 blockage caused by the west coast mountains. On the other hand, the atmosphere over the sea is more stable because
428 the isentropic lines are flatter and denser than Quebec's case, which also favors the development of LLJ. In contrast,
429 the east coast of Quebec is relatively gentle, which may account for its lower wind speed. California's LLJ occurs
430 frequently at each time step, and its diurnal signal is weaker compared, for example, to the signal in the Great Plain
431 S-LLJ. As well, the California signal stays at frequency of over 35%. California's LLJ occurs most frequently at
432 around 18 LST and starts to decline after sunset, which is generally consistent with the coastal baroclinicity.



433
434 **Figure 13. Background circulations of the California coastal N-LLJ in JJA: (a) sea-level pressure, (b) geopotential height**
435 **of 800 hPa, (c) cross section including meridional winds (lines) and potential temperature (shading), and (d) diurnal cycle**

436 of frequency with the shaded 95% confidence intervals. The red lines and points in (a) and (b) show the position of cross-
437 section and chosen jet core, the vertical line in (c) shows the zonal location of the chosen jet core.

438
439 The wind deviations for California's N-LLJ shown in the hodograph (Figure 14a) still have a clockwise rotation in 24
440 hours. However, compared with the magnitude of the daily mean jet-core wind, this diurnal cycle is not quite as
441 obvious as the cycle for Quebec and Great Plain LLJs, but it is similar to the frequency cycle shown in Figure 13d. In
442 comparison between geostrophic and ageostrophic winds (Figure. 14b and 14c), during the afternoon (15 and 18 LST),
443 the amplitude of geostrophic wind is the largest, and the ageostrophic flow diminishes the geostrophic wind. However,
444 in the morning 12 hours later, the relative angle between ageostrophic and geostrophic vectors does not change,
445 meaning that the ageostrophic wind is still weakening the geostrophic wind and that there is no rotation of the
446 ageostrophic wind, as Blackadar inertial oscillation theory describes. Figure 14d helps to explain the change in
447 meridional winds. Looking at the magnitudes of ageostrophic winds, one can see that all are weak and southerly and
448 that they do not exhibit a significant diurnal signal. Furthermore, the change of geostrophic wind is highly consistent
449 with the trend of the actual meridional wind. Thus, the N-LLJ in California can be considered mostly as geostrophic
450 and the diurnal variation as being related to the change in geostrophic winds.



452 **Figure 14. (a) Hodograph of jet-core winds for the California coastal N-LLJ every 3 hours over the whole JJA (red dots –**
453 **solid line) and the daily averaged actual wind velocity (blue vector); vectors of mean jet-core geostrophic winds (solid blue)**
454 **and ageostrophic winds (dashed red) at (b) 15/18 LST and (c) 03/06 LST; (d) diurnal cycles of meridional components of**
455 **actual (black line), geostrophic (blue bars), and ageostrophic winds (red bars).**

456

457 **5 Discussion and conclusion**

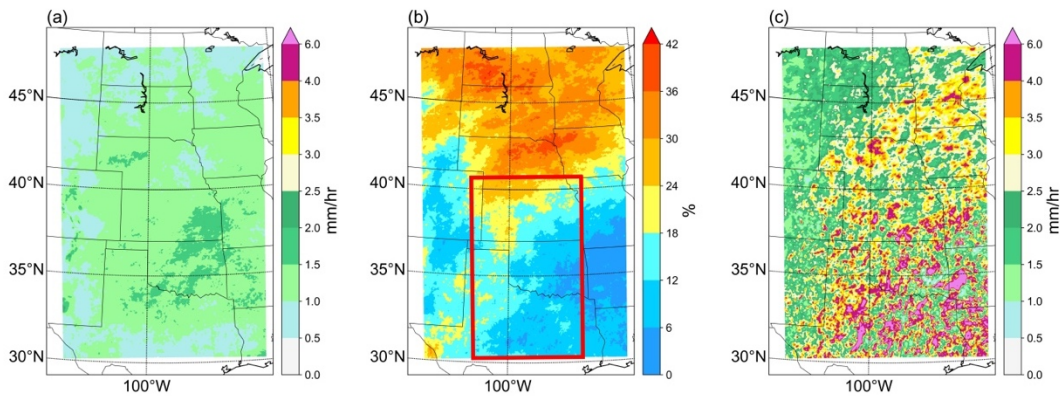
458 This study applied a convection-permitting WRF model to generate the climatology of LLJs in North America. The
459 previous research for LLJs mainly focused on observation data, which have no fine coverage in temporal or spatial
460 resolution. The studies using in-situ observations may ignore some important features. Despite their better coverage,
461 reanalysis datasets usually have a coarse spatial resolution, especially in the vertical direction, and can introduce large
462 inaccuracies in the identification of LLJs. In addition, the application of general numerical modeling cannot avoid the
463 uncertainty caused by parameterizing small-scale physical processes. In contrast, high-resolution convection-
464 permitting climate simulations can provide relatively more comprehensive descriptions of LLJs, especially for areas
465 with complex geographic conditions or regions that lack soundings. Previous studies using high-resolution models
466 conducted case analyses only of LLJs in a specific region (Aird et al., 2022). By expanding the target domain to the
467 whole of North America and revealing the climatological characteristics of LLJs in different regions and scales, this
468 paper provides an accurate reference for future research on LLJ-related processes in North America.

469 The convection-permitting WRF model is able to recapture some LLJs that have been previously studied, such as the
470 Great Plain S-LLJ and the California coastal N-LLJ in the eastern Pacific Ocean and has obtained relatively consistent
471 results. The results indicate that the S-LLJ in the central US Plain is the most frequent and active in warm seasons and
472 that three critical high-frequency centers occur in summer: the northeast Mexico-Texas border, west-central Texas,
473 and western Oklahoma to southern Kansas. This last result is consistent with the climatology generated by Doubler et
474 al. (2015) using the NARR reanalysis data, but the patterns here are more representative of the topographic features
475 in central and southern Texas. In addition, compared with the 40-year rawinsonde climatology in the central US by
476 Walters et al. (2008), our study reveals that the S-LLJ frequency range of these three centers in the central US in
477 summer is 25%-30%, which is slightly lower than the 35% reported in the 2008 study. However, given the
478 underestimated frequencies of 15%-20% in NARR climatology, there is an advantage of using high-resolution
479 simulations in the vertical direction.

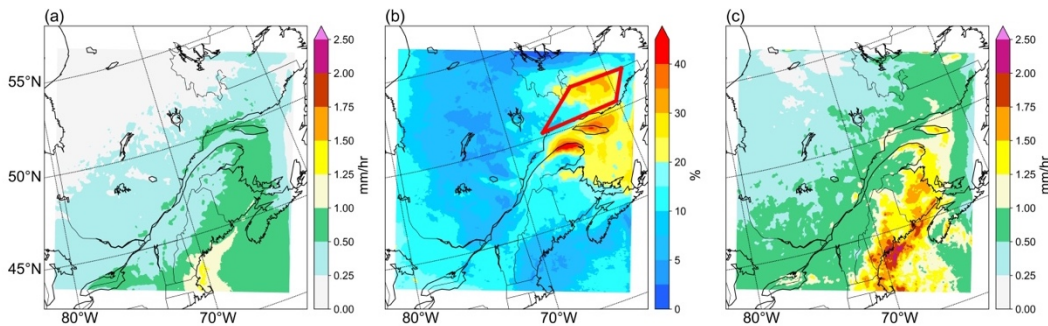
480 The convection-permitting simulation can also capture LLJs that were poorly detected previously using coarser
481 resolution models and observational datasets. The winter N-LLJs over the eastern Rocky Mountains described in this
482 paper are generally distributed over the central US from the Dakotas to Oklahoma with a low frequency (>10%) and
483 over several sporadic small areas with a high frequency (>20%) along the boundary of the Rockies. The main
484 seasonal/diurnal variations identified in this study agree with those seen using rawinsonde data (Walters et al., 2008)
485 and NARR reanalysis (Douber et al., 2015). But the frequency of the LLJ occurrence over Nebraska-Kansas was
486 underestimated in both convection-permitting simulations (~10%) and NARR (~7%), while high-frequency hot spots
487 from Alberta to Colorado were not detected in either of the above-mentioned studies, probably because measurements
488 are lacking in these regions. The high-resolution simulation also detected LLJs on which researchers have hardly
489 focused: N-LLJs near the eastern Quebec coast and in the Appalachians Mountains, as well as an S-LLJ over the
490 British Columbia coast. In the work of Douber et al. (2015), these LLJs were shown in the climatology patterns, but
491 the 4-km WRF simulation offered more detailed descriptions of their locations. For example, this study found that the
492 Appalachian N-LLJ extends from Georgia to the northwestern Atlantic, especially on summer nights (03 UTC – 06
493 UTC), while NARR only captured LLJ occurrences over the middle coast of the Atlantic. The maximum frequency
494 (7-10%) detected in the NARR study is also less than what is illustrated here. As for the Quebec N-LLJ, the 4-km
495 WRF revealed that it mostly occurs onshore near the coast with a frequency of over 25% in winter, but NARR only
496 provided a coarse occurrence distribution over northeastern Canada.

497 To investigate the significance of LLJs in different regions, Figures 15 and 16 demonstrate the impact of the Great
498 Plains S-LLJ and Quebec N-LLJ, respectively, on downstream extreme precipitation during their active seasons.
499 Figure 15a illustrates the 90th percentile of summer precipitation in the central United States, indicating that 90% of
500 the precipitation in most areas falls within the range of 1.0-2.0 mm/hour. However, Figure 15b shows the ratio of
501 strong events related to LLJs (counted if the precipitation is > 90th percentile when a LLJ occurs) to all strong events,
502 with the red outline on the map indicating the approximate location of the low-level jet stream. It is evident that in the
503 lower reaches of the S-LLJ in the Great Plain, particularly in the north-central United States, nearly 50% of the heavy
504 precipitation events are associated with the flourishing low-level jet stream. Furthermore, Figure 15c displays the
505 average precipitation of all LLJ-related strong events. Compared with Figure 15a, some areas of Nebraska and
506 Minnesota experience rainfall of up to 6mm/hour. These findings highlight the significant role played by LLJ in

507 modulating summer precipitation. Similarly, for the Quebec N-LLJ in winter (Fig. 16), it contributes more than 25%
 508 of the strong events of precipitation in the Gulf of St. Lawrence during winter (Fig. 16b). Figure 16c further reveals
 509 that, in comparison to the 90th percentile rainfall, the extreme precipitation from Quebec to Maine is approximately
 510 1mm/hr higher. Particularly during the cold season when a substantial portion of precipitation is snow, the N-LLJs
 511 can also be seen as the factors of snowstorms in this region. In summary, research on the importance of LLJs includes
 512 not only the field of extreme precipitation, but also local wind energy production, air pollution dispersion, wildfires,
 513 etc. (Jain & Flannigan 2021, Lin et al. 2022, Weide Luiz & Fiedler 2022). There is no doubt that the high-resolution
 514 regional climate model presented in this paper provides ample coverage and details about LLJs in North America, to
 515 support analysis in these fields, particularly at the national level. With a grid spacing as small as 4 km, researchers can
 516 even employ the wind profiles from model output to investigate small-scale areas, such as wind farms or wildfire
 517 ignition sites.



518
 519 **Figure 15. (a) 90th percentile of summer precipitation rate over Central US; (b) The ratio of LLJ-related strong rainfall**
 520 **events to all strong events, the red outline represents the location of Great Plain S-LLJ; (c) Averaged precipitation rate of**
 521 **LLJ-related strong events.**



522
 523
 524
 525
 526
 527
 528
 529
 530
 531
 532
 533
 534
 535
 536
 537
 538
 539
 540
 541
 542
 543
 544
 545
 546
 547
 548
 549
 550
 551
 552
 553
 554
 555
 556
 557
 558
 559
 560
 561
 562
 563
 564
 565
 566
 567
 568
 569
 570
 571
 572
 573
 574
 575
 576
 577
 578
 579
 580
 581
 582
 583
 584
 585
 586
 587
 588
 589
 590
 591
 592
 593
 594
 595
 596
 597
 598
 599
 600
 601
 602
 603
 604
 605
 606
 607
 608
 609
 610
 611
 612
 613
 614
 615
 616
 617
 618
 619
 620
 621
 622
 623
 624
 625
 626
 627
 628
 629
 630
 631
 632
 633
 634
 635
 636
 637
 638
 639
 640
 641
 642
 643
 644
 645
 646
 647
 648
 649
 650
 651
 652
 653
 654
 655
 656
 657
 658
 659
 660
 661
 662
 663
 664
 665
 666
 667
 668
 669
 670
 671
 672
 673
 674
 675
 676
 677
 678
 679
 680
 681
 682
 683
 684
 685
 686
 687
 688
 689
 690
 691
 692
 693
 694
 695
 696
 697
 698
 699
 700
 701
 702
 703
 704
 705
 706
 707
 708
 709
 710
 711
 712
 713
 714
 715
 716
 717
 718
 719
 720
 721
 722
 723
 724
 725
 726
 727
 728
 729
 730
 731
 732
 733
 734
 735
 736
 737
 738
 739
 740
 741
 742
 743
 744
 745
 746
 747
 748
 749
 750
 751
 752
 753
 754
 755
 756
 757
 758
 759
 760
 761
 762
 763
 764
 765
 766
 767
 768
 769
 770
 771
 772
 773
 774
 775
 776
 777
 778
 779
 780
 781
 782
 783
 784
 785
 786
 787
 788
 789
 790
 791
 792
 793
 794
 795
 796
 797
 798
 799
 800
 801
 802
 803
 804
 805
 806
 807
 808
 809
 810
 811
 812
 813
 814
 815
 816
 817
 818
 819
 820
 821
 822
 823
 824
 825
 826
 827
 828
 829
 830
 831
 832
 833
 834
 835
 836
 837
 838
 839
 840
 841
 842
 843
 844
 845
 846
 847
 848
 849
 850
 851
 852
 853
 854
 855
 856
 857
 858
 859
 860
 861
 862
 863
 864
 865
 866
 867
 868
 869
 870
 871
 872
 873
 874
 875
 876
 877
 878
 879
 880
 881
 882
 883
 884
 885
 886
 887
 888
 889
 890
 891
 892
 893
 894
 895
 896
 897
 898
 899
 900
 901
 902
 903
 904
 905
 906
 907
 908
 909
 910
 911
 912
 913
 914
 915
 916
 917
 918
 919
 920
 921
 922
 923
 924
 925
 926
 927
 928
 929
 930
 931
 932
 933
 934
 935
 936
 937
 938
 939
 940
 941
 942
 943
 944
 945
 946
 947
 948
 949
 950
 951
 952
 953
 954
 955
 956
 957
 958
 959
 960
 961
 962
 963
 964
 965
 966
 967
 968
 969
 970
 971
 972
 973
 974
 975
 976
 977
 978
 979
 980
 981
 982
 983
 984
 985
 986
 987
 988
 989
 990
 991
 992
 993
 994
 995
 996
 997
 998
 999
 1000

523 **Figure 16. (a) 90th percentile of winter precipitation rate over Southeastern Canada; (b) The ratio of LLJ-related strong**
524 **rainfall events to all strong events, the red outline represents the location of Quebec N-LLJ; (c) Averaged precipitation rate**
525 **of LLJ-related strong events.**

526 Based on the inertial oscillation theory (Blackadar, 1957) and the baroclinic theory near complex terrain (Holton,
527 1967), this paper also analyzed the background and formation mechanisms of three LLJs: the Great Plain S-LLJ,
528 Quebec N-LLJ, and California coastal N-LLJ. Generally, all these LLJs are impacted by the thermodynamic
529 circulations generated near their topography. The Great Plain S-LLJ is affected by slope heating, and the LLJs over
530 Quebec and California are associated with the sea-land contrast. When the geostrophic and ageostrophic components
531 of the LLJs are compared, results show that the inertial oscillation better explains the night enhancement of the Great
532 Plains S-LLJ and that the diurnal feature of the Quebec N-LLJ is influenced by the combination of the Holton and
533 Blackadar theories. As for the California coastal N-LLJ, no supergeostrophic state is found, making coastal
534 baroclinicity variation a dominant factor for this LLJ's evolution the geostrophic wind changes.

535 The LLJs climatology introduced in this research adds to the existing knowledge of characteristics of the low-level
536 wind maxima in North America, thus helping researchers obtain more reliable references about LLJs in this domain.
537 Meanwhile, with the high-resolution features, it can provide more robust explanations for other interdisciplinary fields.
538 The research also advances knowledge about the formation of three dominant LLJs. Although the 13-year simulation
539 is likely too short to provide an ideal long-term climatic analysis, it is a less expensive option for finer numerical
540 modeling in large domains. But it is also believed that with the advancement of technology, there will be longer high-
541 resolution simulations in the future. Future work will address the features and formation mechanisms of the small-
542 scale low-level wind maxima that have yet to be investigated.

543 **Acknowledgments**

544 All authors thank the support of the Global Water Futures Program by the Canada First Research Excellence and the
545 NSERC Discovery Grant.

546

547 **Data Availability Statement**

548 The WRF simulation over CONUS can be accessed at Research Data Archive of NCAR
549 <https://rda.ucar.edu/datasets/ds612.0/>.

550

551 **Author contribution**

552 Xiao Ma: Conceptualization; data curation; formal analysis; investigation; methodology; visualization; writing-
553 original draft.

554 Yanping Li: Conceptualization; funding acquisition; investigation; methodology; project administration; supervision;
555 validation; writing-review and editing.

556 Zhenhua Li: Data curation; methodology; validation; visualization; writing-review and editing.

557 Fei Huo: Data curation; methodology; validation; visualization; writing-review and editing.

558

559 **Competing interests**

560 All authors disclosed no relevant relationships.

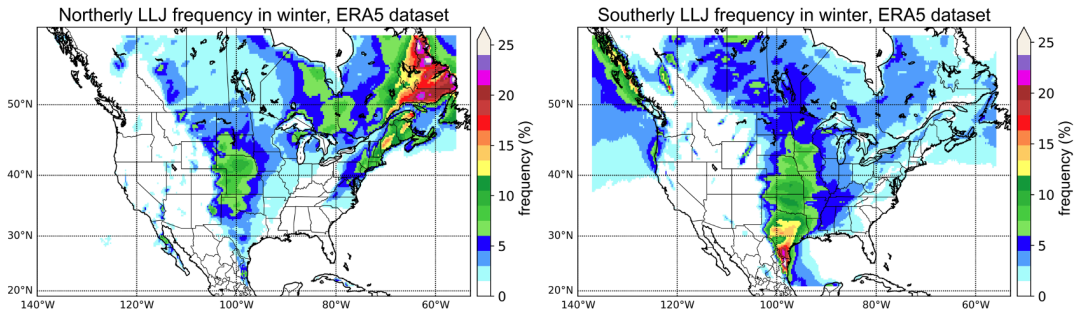
561

562 **Appendix**

563 **Winter LLJs captured by ERA5 Dataset**

564 The convection-permitting WRF simulation exhibited excellent performance in investigating well-known LLJ systems,
565 such as the California coastal N-LLJ and the Great Plains S-LLJ. Moreover, this appendix validates WRF-simulated
566 significant winter jet systems over North America using the ERA5 reanalysis dataset. ERA5 is a global atmospheric
567 reanalysis dataset produced by the European Centre for Medium-Range Weather Forecasts (ECMWF). It provides
568 hourly data on a horizontal grid space of approximately 31 km, and the time range covers from 1979 till the present.
569 ERA5 data is widely used in climate research, weather forecasting, and various applications that require high-quality
570 atmospheric data.

571 The validation period is the same as the WRF simulation (2000-2013). From the Figure A1 below, it is evident that
572 during winter, a greater number of significant N-LLJ systems in the North American continent are mostly concentrated
573 in eastern Canada. In most parts of Newfoundland and southeastern Quebec, the occurrence frequency of N-LLJs
574 exceeds 15%, and the maximum can even surpass 25%. However, in the WRF simulation (Figure 3d), the model can
575 only capture N-LLJs on the north bank of the St. Lawrence River due to the northern boundary of the study domain
576 overlapping with the Quebec border. In comparison, the WRF-simulated frequency of N-LLJs in southeastern Quebec
577 essentially exceeds 25%, overestimated by about 5% compared to the ERA5 reanalysis. Additionally, it is worth noting
578 that the N-LLJs along the downstream of Rockies are also identified in the ERA5 dataset. The areas where the
579 frequency exceeds 5% are mainly distributed from Alberta to northern Texas, consistent with the findings in Section
580 3.2.1. Moreover, the high-value center (>10%) is located in central Kansas. In terms of the differences between the
581 two datasets, the results of the WRF simulation match more geographical features and reveal scattered high-value
582 spots (>15%) in some regions with special terrains (see Figure 3d). Furthermore, the winter Great Plains S-LLJs in
583 ERA5 reanalysis exhibit similar features, with frequencies ranging from around 15% to 20% in southern Texas. In
584 summary, the WRF model can accurately capture the features of winter LLJ systems, which are validated by the ERA5
585 reanalysis dataset over northern America. Even though the frequency of LLJs occurrence is overestimated, the
586 convection-permitting WRF simulation can provide detailed descriptions of LLJs near complex terrains.



587

588 **Figure A1. Winter occurrence frequency of N-LLJs (left) and S-LLJs (right).**

589

590

591

592 **Data Availability Statement**

593 The ERA5 dataset is available on the Copernicus Climate Change Service Information website.

594 <https://cds.climate.copernicus.eu/#!/home>

595

596

597 **References**

- 598 Aird, J. A., Barthelmie, R. J., Shepherd, T. J. and Pryor, S. C.: Occurrence of Low-Level Jets over the Eastern U.S.
599 Coastal Zone at Heights Relevant to Wind Energy, *Energies*, 15(2), 445, doi:10.3390/en15020445, 2022.
- 600 Blackadar, A. K.: Boundary Layer Wind Maxima and Their Significance for the Growth of Nocturnal Inversions,
601 *Bulletin of the American Meteorological Society*, 38(5), 283–290, doi:10.1175/1520-0477-38.5.283, 1957.
- 602 Bonner, W. D.: CLIMATOLOGY OF THE LOW LEVEL JET, *Monthly Weather Review*, 96(12), 833–850,
603 doi:10.1175/1520-0493(1968)096<0833:cotllj>2.0.co;2, 1968.
- 604 Chen, G. T.-J., Wang, C.-C. and Lin, D. T.-W.: Characteristics of Low-Level Jets over Northern Taiwan in Mei-Yu
605 Season and Their Relationship to Heavy Rain Events, *Monthly Weather Review*, 133(1), 20–43, doi:10.1175/mwr-
606 2813.1, 2005.
- 607 Doubler, D. L., Winkler, J. A., Bian, X., Walters, C. K. and Zhong, S.: An NARR-Derived Climatology of Southerly
608 and Northerly Low-Level Jets over North America and Coastal Environs, *Journal of Applied Meteorology and*
609 *Climatology*, 54(7), 1596–1619, doi:10.1175/jamc-d-14-0311.1, 2015.
- 610 Du, Y. and Chen, G.: Heavy Rainfall Associated with Double Low-Level Jets over Southern China. Part II: Convection
611 Initiation, *Monthly Weather Review*, 147(2), 543–565, doi:10.1175/mwr-d-18-0102.1, 2019.
- 612 Frisch, A. S., Orr, B. W. and Martner, B. E.: Doppler Radar Observations of the Development of a Boundary-Layer
613 Nocturnal Jet, *Monthly Weather Review*, 120(1), 3–16, doi:10.1175/1520-
614 0493(1992)120<0003:drootd>2.0.co;2, 1992.
- 615 Fu, P., Zhu, K., Zhao, K., Zhou, B. and Xue, M.: Role of the nocturnal low-level jet in the formation of the morning
616 precipitation peak over the Dabie Mountains, *Advances in Atmospheric Sciences*, 36(1), 15–28, doi:10.1007/s00376-
617 018-8095-5, 2018.
- 618 Gadde, S. N. and Stevens, R. J. A. M.: Effect of low-level jet height on wind farm performance, *Journal of Renewable*
619 *and Sustainable Energy*, 13(1), 013305, doi:10.1063/5.0026232, 2021.

620 Hodges, D. and Pu, Z.: Characteristics and Variations of Low-Level Jets and Environmental Factors Associated with
621 Summer Precipitation Extremes over the Great Plains, *Journal of Climate*, 32(16), 5123–5144, doi:10.1175/jcli-d-18-
622 0553.1, 2019.

623 Hoffmann, L. and Spang, R.: An assessment of tropopause characteristics of the ERA5 and era-interim meteorological
624 reanalyses, *Atmospheric Chemistry and Physics*, 22(6), 4019–4046, doi:10.5194/acp-22-4019-2022, 2022.

625 Holton, J. R.: The diurnal boundary layer wind oscillation above sloping terrain, *Tellus*, 19(2), 199–205,
626 doi:10.1111/j.2153-3490.1967.tb01473.x, 1967.

627 Hong, S.-Y., Noh, Y. and Dudhia, J.: A New Vertical Diffusion Package with an Explicit Treatment of Entrainment
628 Processes, *Monthly Weather Review*, 134(9), 2318–2341, doi:10.1175/mwr3199.1, 2006.

629 Hu, X.-M., Klein, P. M., Xue, M., Lundquist, J. K., Zhang, F. and Qi, Y.: Impact of Low-Level Jets on the Nocturnal
630 Urban Heat Island Intensity in Oklahoma City, *Journal of Applied Meteorology and Climatology*, 52(8), 1779–1802,
631 doi:10.1175/jamc-d-12-0256.1, 2013.

632 Iacono, M. J., Delamere, J. S., Mlawer, E. J., Shephard, M. W., Clough, S. A. and Collins, W. D.: Radiative forcing
633 by long-lived greenhouse gases: Calculations with the AER radiative transfer models, *Journal of Geophysical*
634 *Research*, 113(D13), doi:10.1029/2008jd009944, 2008.

635 Jain, P. and Flannigan, M.: The relationship between the Polar Jet Stream and extreme wildfire events in North
636 America, *Journal of Climate*, 1–59, doi:10.1175/jcli-d-20-0863.1, 2021.

637 Jiménez-Sánchez, G., Markowski, P. M., Jewtoukoff, V., Young, G. S. and Stensrud, D. J.: The Orinoco Low-Level
638 Jet: An Investigation of Its Characteristics and Evolution Using the WRF Model, *Journal of Geophysical Research:*
639 *Atmospheres*, 124(20), 10696–10711, doi:10.1029/2019jd030934, 2019.

640 Kurkute, S., Li, Z., Li, Y. and Huo, F.: Assessment and projection of the water budget over Western Canada using
641 convection-permitting weather research and forecasting simulations, *Hydrology and Earth System Sciences*, 24(7),
642 3677–3697, doi:10.5194/hess-24-3677-2020, 2020.

643 Li, Y., Li, Z., Zhang, Z., Chen, L., Kurkute, S., Scaff, L. and Pan, X.: High-resolution regional climate modeling and
644 projection over Western Canada using a weather research forecasting model with a pseudo-global warming approach,
645 *Hydrology and Earth System Sciences*, 23(11), 4635–4659, doi:10.5194/hess-23-4635-2019, 2019.

646 Lin, Y., Wang, C., Yan, J., Li, J. and He, S.: Observation and simulation of low-level jet impacts on 3D urban heat
647 islands in Beijing: A case study, *Journal of the Atmospheric Sciences*, 79(8), 2059–2073, doi:10.1175/jas-d-21-0245.1,
648 2022.

649 Liu, C., Ikeda, K., Rasmussen, R., Barlage, M., Newman, A. J., Prein, A. F., Chen, F., Chen, L., Clark, M., Dai, A.,
650 Dudhia, J., Eidhammer, T., Gochis, D., Gutmann, E., Kurkute, S., Li, Y., Thompson, G. and Yates, D.: Continental-
651 scale convection-permitting modeling of the current and future climate of North America, *Climate Dynamics*, 49(1–
652 2), 71–95, doi:10.1007/s00382-016-3327-9, 2016.

653 Ma, X., Li, Y. and Li, Z.: The projection of Canadian wind energy potential in future scenarios using a convection-
654 permitting regional climate model, *Energy Reports*, 8, 7176–7187, doi:10.1016/j.egyr.2022.05.122, 2022.

655 Miao, Y., Guo, J., Liu, S., Wei, W., Zhang, G., Lin, Y., Zhai, P., Zhai, P., Lin, Y., Zhang, G., Wei, W., Liu, S., Guo,
656 J. and Miao, Y.: The Climatology of Low-Level Jet in Beijing and Guangzhou, China, *Journal of Geophysical*
657 *Research: Atmosphere*, 123(5), 2816–2830, doi:10.1002/2017jd027321, 2018.

658 Mitchell, M. J., Arritt, R. W. and Labas, K.: A Climatology of the Warm Season Great Plains Low-Level Jet Using
659 Wind Profiler Observations, *Weather and Forecasting*, 10(3), 576–591, doi:10.1175/1520-
660 0434(1995)010<0576:acotws>2.0.co;2, 1995.

661 Montini, T. L., Jones, C. and Carvalho, L. M. V.: The South American Low-Level Jet: A New Climatology, Variability,
662 and Changes, *Journal of Geophysical Research: Atmospheres*, 124(3), 1200–1218, doi:10.1029/2018jd029634, 2019.

663 Munday, C., Washington, R. and Hart, N.: African Low-Level Jets and Their Importance for Water Vapor Transport
664 and Rainfall, *Geophysical Research Letters*, 48(1), doi:10.1029/2020gl090999, 2021.

665 Niu, G.-Y., Yang, Z.-L., Mitchell, K. E., Chen, F., Ek, M. B., Barlage, M., Kumar, A., Manning, K., Niyogi, D.,
666 Rosero, E., Tewari, M. and Xia, Y.: The community Noah land surface model with multiparameterization options
667 (Noah-MP): 1. Model description and evaluation with local-scale measurements, *Journal of Geophysical Research*,
668 116(D12), doi:10.1029/2010jd015139, 2011.

669 Parish, T. R.: Forcing of the Summertime Low-Level Jet along the California Coast, *Journal of Applied Meteorology*,
670 39(12), 2421–2433, doi:10.1175/1520-0450(2000)039<2421:fotsll>2.0.co;2, 2000.

671 Rahn, D. A. and Parish, T. R.: Diagnosis of the Forcing and Structure of the Coastal Jet near Cape Mendocino Using
672 In Situ Observations and Numerical Simulations, *Journal of Applied Meteorology and Climatology*, 46(9), 1455–1468,
673 doi:10.1175/jam2546.1, 2007.

674 Rife, D. L., Pinto, J. O., Monaghan, A. J., Davis, C. A. and Hannan, J. R.: Global Distribution and Characteristics of
675 Diurnally Varying Low-Level Jets, *Journal of Climate*, 23(19), 5041–5064, doi:10.1175/2010jcli3514.1, 2010.

676 Saulo, C., Ruiz, J. and Skabar, Y. G.: Synergism between the Low-Level Jet and Organized Convection at Its Exit
677 Region, *Monthly Weather Review*, 135(4), 1310–1326, doi:10.1175/mwr3317.1, 2007.

678 Shapiro, A., Fedorovich, E. and Rahimi, S.: A unified theory for the Great Plains Nocturnal low-level jet, *Journal of*
679 *the Atmospheric Sciences*, 73(8), 3037–3057, doi:10.1175/jas-d-15-0307.1, 2016.

680 Smith, E. N., Gebauer, J. G., Klein, P. M., Fedorovich, E. and Gibbs, J. A.: The Great Plains Low-Level Jet during
681 PECAN: Observed and Simulated Characteristics, *Monthly Weather Review*, 147(6), 1845–1869, doi:10.1175/mwr-
682 d-18-0293.1, 2019.

683 Soares, P. M., Lima, D. C., Semedo, A., Cardoso, R. M., Cabos, W. and Sein, D. V.: Assessing the climate change
684 impact on the North African offshore surface wind and coastal low-level jet using coupled and uncoupled regional
685 climate simulations, *Climate Dynamics*, 52(11), 7111–7132, doi:10.1007/s00382-018-4565-9, 2018.

686 Stensrud, D. J.: Importance of Low-Level Jets to Climate: A Review, *Journal of Climate*, 9(8), 1698–1711,
687 doi:10.1175/1520-0442(1996)009<1698:iolljt>2.0.co;2, 1996.

688 Sullivan, J. T., Rabenhorst, S. D., Dreessen, J., McGee, T. J., Delgado, R., Twigg, L. and Sumnicht, G.: Lidar
689 observations revealing transport of O₃ in the presence of a nocturnal low-level jet: Regional implications for “next-
690 day” pollution, *Atmospheric Environment*, 158, 160–171, doi:10.1016/j.atmosenv.2017.03.039, 2017.

691 Tang, Y., Winkler, J., Zhong, S., Bian, X., Doubler, D., Yu, L. and Walters, C.: Future changes in the climatology of
692 the Great Plains low-level jet derived from fine resolution multi-model simulations, *Scientific Reports*, 7(1),
693 doi:10.1038/s41598-017-05135-0, 2017.

694 Uccellini, L. W., Petersen, R. A., Kocin, P. J., Brill, K. F. and Tuccillo, J. J.: Synergistic Interactions between an
695 Upper-Level Jet Streak and Diabatic Processes that Influence the Development of a Low-Level Jet and a Secondary
696 Coastal Cyclone, *Monthly Weather Review*, 115(10), 2227–2261, doi:10.1175/1520-
697 0493(1987)115<2227:sibaul>2.0.co;2, 1987.

698 Van de Wiel, B. J., Moene, A. F., Steeneveld, G. J., Baas, P., Bosveld, F. C. and Holtslag, A. A.: A conceptual view
699 on inertial oscillations and nocturnal low-level jets, *Journal of the Atmospheric Sciences*, 67(8), 2679–2689,
700 doi:10.1175/2010jas3289.1, 2010.

701 Walters, C. K. and Winkler, J. A.: Airflow Configurations of Warm Season Southerly Low-Level Wind Maxima in
702 the Great Plains. Part I: Spatial and Temporal Characteristics and Relationship to Convection, *Weather and*
703 *Forecasting*, 16(5), 513–530, doi:10.1175/1520-0434(2001)016<0513:acowss>2.0.co;2, 2001.

704 Walters, C. K., Winkler, J. A., Shadbolt, R. P., van Ravensway, J. and Bierly, G. D.: A Long-Term Climatology of
705 Southerly and Northerly Low-Level Jets for the Central United States, *Annals of the Association of American*
706 *Geographers*, 98(3), 521–552, doi:10.1080/00045600802046387, 2008.

707 Weide Luiz, E. and Fiedler, S.: Spatiotemporal observations of nocturnal low-level jets and impacts on wind
708 power production, *Wind Energy Science*, 7(4), 1575–1591, doi:10.5194/wes-7-1575-2022, 2022.

709 Zhang, Y., Xue, M., Zhu, K. and Zhou, B.: What is the main cause of diurnal variation and nocturnal peak of summer
710 precipitation in Sichuan Basin, China? the key role of boundary layer low-level jet inertial oscillations, *Journal of*
711 *Geophysical Research: Atmospheres*, 124(5), 2643–2664, doi:10.1029/2018jd029834, 2019.

712 Zhong, S., Fast, J. D. and Bian, X.: A Case Study of the Great Plains Low-Level Jet Using Wind Profiler Network
713 Data and a High-Resolution Mesoscale Model, *Monthly Weather Review*, 124(5), 785–806, doi:10.1175/1520-
714 0493(1996)124<0785:acsotg>2.0.co;2, 1996.